The Thesis Committee for Shadya Taleb Restrepo
Certifies that this is the approved version of the following Thesis:

Investigation of CO_2 Migration in Saline Aquifers Using Real-Rock Microfluidic Experiments

APPROVED BY
SUPERVISING COMMITTEE:

Seyyed A. Hosseini, Supervisor

Susan D. Hovorka

Sahar Bakhshian

Investigation of CO_2 Migration in Saline Aquifers Using Real-Rock Microfluidic Experiments

by

Shadya Taleb Restrepo

Thesis

Presented to the Faculty of the Graduate School of

The University of Texas at Austin

in Partial Fulfillment

of the Requirements

for the Degree of

Master of Science in Energy and Earth Resources

The University of Texas at Austin

December 2023

Dedication

I dedicate this thesis to my family, for guiding me and encouraging me to always accomplish more. To my husband, whose solid support and inspiration have been the foundation of my academic journey. This achievement is as much yours as it is mine. I am deeply grateful for your scientific insights, strength, and courage you have provided these years.

Acknowledgements

I am deeply grateful to the Department of Energy for funding my thesis through the GOMCARB Project: "Partnership for Offshore Carbon Storage Resources and Technology Development in the Gulf of Mexico", project number DE-FE0031558. This funding enabled me to pursue research in this critical field. I also want to acknowledge the Jackson School of Geosciences Equipment Funding for providing support to obtain the Isco Pump (Model 260x) and Chevron for funding the Zeiss Stemi 508 Stereo Microscope.

I would like to express my gratitude to my advisor, Seyyed Hosseini. Thank you Seyyed for your guidance, expertise, and constant belief in my abilities. Special thanks to Susan Hovorka, for opening the doors to the world of carbon capture and storage (CCS). I am grateful for your mentorship and for the opportunity to contribute to meaningful research. I extend my appreciation to Sahar Bakhshian, for her valuable insights, ideas, and constructive feedback.

I express my thanks to the members of the Gulf Coast Carbon Center (GCCC) for engaging conversations and insights, contributing to a great intellectual environment. Special thanks to Hailun (and Jose), for her technical support, willingness to answer questions and for their assistance with test materials, such as analog fluids and rock samples. I would like to acknowledge Richard Larson for his assistance in setting up the lab and providing help with materials and tools. Also, my sincere thanks to the BEG Core Repository team, particularly Nate and Brandon, for their dedicated support with cores and tools.

I extend my appreciation to the Energy and Earth Resources program and the Jackson School of Geosciences for providing an excellent education and encouraging an environment that contributes to great research and learning.

Abstract

Investigation of CO_2 Migration in Saline Aquifers Using Real-Rock Microfluidic Experiments

Shadya Taleb Restrepo, MS in Energy and Earth Resources

The University of Texas at Austin, 2023

Supervisor: Seyyed A. Hosseini

Over the past decade, reducing carbon dioxide (CO_2) emissions has become critical to tackle climate change and its impacts on human life. While several efforts are being made worldwide to reduce emission levels, geological carbon storage represents a viable technology to sequester CO_2 from large-scale emission sources that are hard to abate. However, the injection of CO_2 into subsurface porous rocks is a complex process and understanding multiphase flow processes is critical for the long-term and short-term assessment of the stored CO_2. This thesis focuses on understanding of CO_2 migration at the pore scale. Synthetic microfluidic models allow precise control of the pore topology; however, they fail to reproduce rock-fluid interactions and cannot capture the effects of heterogeneous mineral distribution. I use real-rock microfluidic devices made of sandstone to estimate the saturation of trapped CO_2 in a brine-saturated porous medium. I first present the micromodel fabrication methodology that combines rock thin sections with nanofabrication techniques (e.g., soft lithography). Images obtained during the experiments are used to detect the phase saturation of each fluid in the micromodel. Then,

I obtain capillary pressure curves using the wetting-phase saturations and peripheral pressure measurements. I conducted fluid flow experiments under dynamic conditions using sandstone samples from Cranfield, Mississippi (Lower Tuscaloosa Formation) and commercial lab samples of Berea sandstone from Ohio and used analog fluids to match the supercritical CO_2 and brine properties. Our experimental results heavily depend on the injection flow rate of the supercritical CO_2 analog; however, for Tuscaloosa samples, when normalized with flow rate, the capillary pressure curves collapse into a single trend. Our experimental results were compared with core-scale measurements. While the two techniques successfully compare for the tests conducted here, it is important to consider the scale of heterogeneities present in the rock. Micromodel-based capillary pressure determination is a useful approach when the size of the heterogeneities is smaller than the micromodel size.

Table of Contents

List of Tables

List of Figures

Chapter 1: Introduction

The reduction of greenhouse gas emissions has become paramount for the public, governments, industry and scientific community in the past years. Global energy consumption will increase in the next decades and the use of fossil fuels will satisfy energy demand growth from emerging and developing economies (IEA, 2021). CO_2 annual emissions into the atmosphere have increased around 100 times faster compared to typical non-anthropogenic rates seen during the end of the last ice age (NOAA, 2021). Therefore, the need to mitigate CO_2 emissions is critical for a sustainable energy strategy.

Several efforts are being made worldwide to decrease CO_2 emission levels. These include the increase in energy efficiency (Brown and Li, 2019), the use of renewable energies (Panwar et al., 2011), and the recycling of resources (Bostanci et al., 2018). While these strategies are undergoing continuous development, their applicability to large-scale scenarios is limited for both, current and projected emission levels. For processes in which technology has not reached low-emission substitutes yet, Geological Carbon Sequestration (GCS) is an alternative. GCS is the process of injecting CO_2 in the subsurface for long-term and secure storage. Particularly, deep saline aquifers have been proposed as being an effective option for large scale geological CO_2 storage (Bachu, S. 2003), with field tests showing the CO_2 storage ability in these systems (Hovorka et al., 2006). While there are numerous examples of CO_2 accumulated and stored in fields and in high CO_2 methane accumulations (e.g., Sleipner and Frio (Aminu et al., 2017)), there are no physical analogues that show the long-term capacity of saline aquifers to safely store anthropogenic CO_2 where these is no structural trap. Thus, there is a need to study, understand and predict how the target injection zones will trap the CO_2 (Bruant et al., 2002).

GCS is assessed at a large-scale and there are different CO_2 trapping mechanisms involved in GCS. These mechanisms are processes that ensure the storage of the CO_2 after injection (Han et al., 2010). The stratigraphic (or structural) trapping is the main mechanism (also called primary trapping), and it involves the immobilization of CO_2 caused by the confinement in a low permeability sequence (Lu et al., 2013). Secondary trapping mechanisms involve mineral trapping, dissolution trapping, and residual/capillary trapping (Bakhshian and Hosseini, 2021).

Carbon dioxide storage capacity depends on various physical properties and processes that happen over different time and length scales. The "static capacity" considers the volume of the reservoir and the effective porosity modified by a storage efficiency factor to provide an upper bound for the amount of CO_2 that can be stored in a geological system (Van der Meer, 1995). The "dynamic capacity" includes the effects of the CO_2 dynamic flow behavior and formation pressure response over injection time. In this case, the brine volume displaced by the CO_2 and pore-scale displacement efficiency may drastically affect the amount of CO_2 stored underground (Riazi et al, 2011). These phenomena are controlled by rock and fluid properties such as capillary pressure and relative permeability. Thus, pore-scale phenomena play a critical role in the CO_2 distribution and flow behavior in the subsurface.

The injection of CO_2 in saline aquifer formations involves complex multiphase fluid flow processes. For example, buoyancy and pressure gradients drive CO_2 flow, displacing in-situ fluids (i.e., brine) in the near-wellbore region (Kim et al., 2012). Far from the injection well, viscous forces decrease, and the interaction of capillary and gravity forces become dominant (Berg and Ott, 2012). In both cases, the non-wetting phase (CO_2), displaces the wetting phase (brine). This type of fluid displacement is known as drainage

(Lenormand et al., 1998). At some locations, brine returns back into some of the CO_2 invaded pore space, causing part of that CO_2 to become residually trapped in the pore space (Abdoulghafour et al., 2020). In this scenario, the wetting phase (brine) displaces the non-wetting phase (CO_2), a process known as imbibition (Blunt, 2017). The residual trapping of the CO_2 is intimately related to the capillary pressure characteristics of the rock and fluids. Thus, a reliable capillary pressure must be used to model CO_2-brine injections at reservoir scale.

Capillary pressure (Pc) is the pressure difference between the wetting and non-wetting fluid (Gray et al., 2019). In porous media, it is predominantly controlled by pore geometry, pore size and heterogeneity, and the type of fluids present (Aryana and Kovscek, 2012). When injected CO_2 invades the pores of an aquifer, capillary forces allow only a fraction of the carbon dioxide to invade the pores, the larger pores with lower capillary entry pressure get invaded first, followed by smaller pores with higher capillary entry pressures, but not all the pores get invaded because of the high capillary pressure, which causes a residual saturation of the brine (Chen, 2015). The magnitude of the capillary forces is determined by the pore size distribution in the rock and consequently, the residual saturation will also depend on the rock and fluid characteristics (Tong et al., 2006).

Previous investigations have demonstrated how capillary pressure affects CO_2 plume migration and storage security. Gershenzon et al. (2016) compared CO_2 trapping in highly heterogenous reservoirs and observed how the geological heterogeneities at pore-scale control capillary pressure curves and consequently, affect the large-scale characteristics of the CO_2 plume. Efforts have been dedicated to develop dynamic models that capture the impact of the macroscale capillary pressure in geologic CO_2 storage (Kassa et al., 2020). These advances quantify CO_2 trapping using modeling and experimental tests

to support numerical simulation predictions for future CO_2 storage prospects in saline aquifers.

Experimental techniques including core-flooding experiments have been used to study how the capillary heterogeneity influences the residual trapping of CO_2 in a brine-saturated system (Krevor et al., 2011), however, visualization at the pore-scale has been limited. Micromodels offer direct visualization of the pore-scale processes; nonetheless, they have been manufactured using engineered materials (e.g., silicon or glass). Sandstone rock microscopic experiments have not been performed to investigate capillary pressure curves measurements in GCS.

This thesis investigates capillary pressure curves by using pore-scale experiments through sandstones-like microfluidics devices at different injection rates and various sandstone rocks. This thesis also presents a novel methodology to perform laboratory experiments on microfluidics devices representative of geologic structures by using real rocks. Results obtained from these experiments will allow to characterize and eventually optimize macroscale capillary pressure estimations by matching experimental results with pore-scale modeling data. These studies of flow dynamics using microfluidics techniques and numerical methods play an important role in the development of future subsurface storage technologies, because they will allow to validate capillary pressure values obtained to predict multiphase flow migration processes at reservoir-scale.

Chapter 2: Background and Literature Review

2.1. PREVIOUS MICROFLUIDIC STUDIES FOR GEOLOGICAL CARBON STORAGE APPLICATIONS

Micromodel devices are synthetic representations of porous media and consist of pores bodies and pore-throats that are designed according to the purpose of each study. The pattern design determines the size of the pore bodies and the width of the pore-throats. (Lenormand et al, 1983). Different patterns have been used in studies that involve CO_2 and the features change to contribute to the physics of the processes of interest. One of the first micromodel experiments involving high pressure CO_2 injection, was developed to evaluate oil recovery, the study was performed by Campbell and Orr in 1985, they fabricated homogeneous and heterogeneous patterns etched in glass to evaluate the oil displacement in the absence of water and in different pore distributions.

CO_2 is injected into the subsurface at supercritical conditions; thus, CO_2 microfluidic studies require high pressure and temperature. Fabrication materials are sought to emulate these conditions, and test protocols are designed considering the objective of the study, fluid conditions, and pore size effects. Table 1 summarizes previous microfluidics studies for GCS applications. Although the emphasis is on GCS, most of these developments in fabrication techniques and experimental methodologies are developed for EOR studies.

Microfluidics experiments include a fluid injection system, imaging equipment and micromodel devices. Important improvements in imaging, computational sciences and micromodel fabrication have contributed significantly to the understanding of multiphase CO_2 flow and transport phenomena in porous media (Armstrong et al., 2016).

Author / Year	Fabrication material	Type of study	Model Size (mm^2)	Depth (μm)	Porosity (%)	Pressure (MPa)	Temperature (°C)	Avg Injection rate (mL/min)
Campbell and Orr., 1985	Glass	Displacement mechanisms	2,552	200	-	8.3	-	0.011 - 0.0175
Sayegh and Fisher., 2009	Glass	Displacement mechanisms	825	35	65	10	50	0.1 - 1
Cinar et al., 2009	Glass	Invasion patterns	29,205	11	-	-	-	0.44 – 6.5
Er et al., 2010	Glass	Wettability	1,000	40	-	10.3	-	0.83 - 2.5
Riazi et al., 2011	Glass	Displacement mechanisms	280	50	62	13.8	38	-
Zhang et al., 2011	Silicon	Fingering effects	1.47	35	39.87	9	22	0.0016 - 0.16
Zhang et al., 2011	Silicon	Fingering effects	450	53	39	0.1	22	0.000083 - 0.125
Buchgraber et al., 2012	Silicon	Fabrication technique or disp.	1.51	25	46	0.9	-	-
Buchgraber et al., 2012	Silicon	CO_2 dissolution	2500	25	46	7.9	44.4	0.001 - 0.1
Kim et al., 2012	Silicon	Salt precipitation	200	40	-	8.5	45	0.004
Sell. A., 2012	Polymer	CO_2 diffusivity	625	50	-	5	26	-
Wang et al., 2013	Silicon	Fingering effects	1.44	35	40	9	41	125
Zuo et al., 2013	Silicon	CO_2 exsolution	37.63	35	35	9	45	-
Kazemifar et al., 2015	Silicon	Displacement mechanisms	156.25	30	51	8	23	0.005
Miri et al., 2015	Glass	Salt precipitation	50	350	-	0.1	22	-
Kazemifar et al., 2016	Silicon	Displacement mechanisms	156.25	30	50.5	8	40	0.005
Mahdavi et al., 2016	Glass	Displacement mechanisms	13500	-	30	2.1	21	-
Porter et al., 2016	Geomaterial	Fabrication technique	1219	-	-	8.6	50	0.1
Chang et al., 2017	Silicon	CO_2 dissolution	37.63	35	35	9	40	0.042
Hu et al., 2017	Silicon	Wettability	200	40	24.5	8.5	45	0.48 - 1
Jafari and Jung., 2017	Glass	Contact angle	200	20		8	21	0.0001
Li et al., 2017	Silicon	Displacement mechanisms	37.63		51	8	21	0.005 - 0.05
Chen, et al., 2018	Silicon	Invasion patterns	37.63	30	51	8.6	-	-
Fakhari et al., 2018	Silicon	Invasion patterns	37.63	30	49.5	8.4	21	0.05 - 0.25
Chang et al., 2019	Silicon	CO_2 dissolution	37.63	37	35	9	40	0.0083
He et al., 2019	Glass	Salt precipitation	400	45	39.1	10	50	0.1 - 2
Jafari and Jung., 2019	Glass	Contact angle	200	20	-	8	23	0.0001
Nooraiepour et al., 2019	Geomaterial	Salt precipitation	6.25	-	30	8	60	20
Seo et al., 2019	Polymer	CO_2 dissolution	-	1500	-	0.1	25	7080
Mahdavi and James., 2020	Glass	Displacement mechanisms	-	-	-	2.1	21	-
Lv et al., 2020	Glass	Displacement mechanisms	2342.7	900	30	8	40	0.003 - 0.1
Jadhawar et al., 2020	Glass	Displacement mechanisms	-	-	-	8.3	-	-
Dimou et al., 2021	Resin (3D)	Fabrication technique	2	1000	-	-	-	0.5
Li et al., 2021	Silicon	Displacement mechanisms	78.54	30	44	8	21	0.005
Lu et al., 2021	Silicon	CO_2 exsolution	44.55	30	32.6	9	50	0.0001 - 0.1
Amarasinghe et al., 2021	Glass	Displacement mechanisms	358.4	40	61	10	50	0.08 - 0.00017

Table 1: Published micromodel studies involving CO_2 injection, ordered chronologically. The studies are categorized by study type and the columns present the properties of the models and flow conditions of each test. Empty cells correspond to data that was not reported.

A few of the CO_2 sequestration microfluidics studies listed in Table 1 been applied to the study of CO_2 storage in saline aquifers. For example, Riatzi et al. (2011) injected CO_2 as the non-wetting phase, displacing the brine (wetting phase) in the micromodel. This non-wetting fluid injection corresponds to a drainage process. Similarly, other studies have investigated the impact of different pore characteristics by changing grain size distribution and porosity (Fig. 1). For example, Chang et al. (2019) studied CO_2 injection during imbibition using four different micromodels to evaluate the impact of pore size distribution on flow behavior.

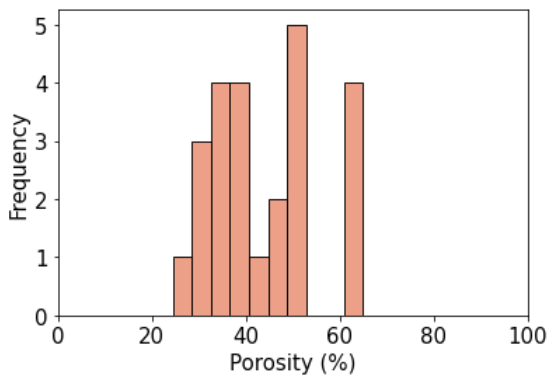

Figure 1: Porosity values from the micromodel devices used in CO_2 injection studies listed in Table 1.

2.1.1. Displacement mechanisms and fingering effects

Understanding how the CO_2 displaces in-situ fluids (i.e., displacement mechanisms) and flow fingering effects is crucial for successful and effective GCS. The efficiency of the displacement mechanism can impact the effectiveness of the CO_2 to replace the formation in situ fluids, as well as the long-term stability of the storage site.

Pore-scale studies are complemented with core-scale experiments. Lv et al. (2020) combined core-flooding and micromodel experiments to evaluate the effects of

heterogeneous porosity at the pore and core scales. They observed how disordered pore sizes affect capillary, gravitational and viscous forces. Other studies focused on capillary and viscous fingering. For example, Zhang et al. (2011) fabricated dual-permeability micromodels and investigated the transition from capillary to viscous fingering with increasing flow rate and permeability contrasts (Fig. 2). Wang et al. (2013) investigated unstable displacement mechanisms for CO_2-water systems at pore-scale using a homogeneous silicon device at different continuous and discontinuous injection rates. The authors observed that capillary fingering was dominant for the tested injection rates, which results in an increase of trapped CO_2 saturation.

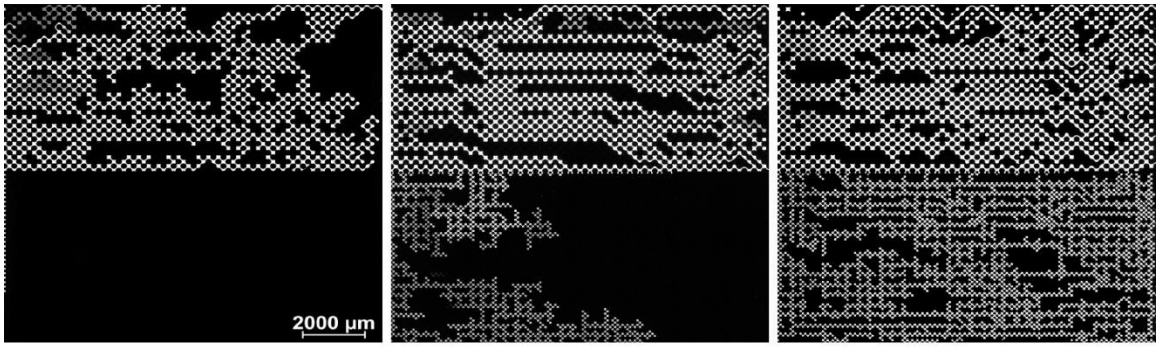

log*Ca* = -4.96 -3.66 -3.36

Figure 2: Liquid CO_2 distribution in a dual-permeability micromodel at different injection rates (Zhang et al., 2011).

Sayegh and Fisher (2008) develop a model to generate a 2D pore network that represents a porous media, controlling grain size and shape. Then, the authors used this model to fabricate a glass micromodel, where they studied the recovery of oil at high pressure and temperature during CO_2 injection and water-gas co-injection. They observed that fingering was the dominant displacement mechanism in all the CO_2 floods and also observed a higher oil recovery when CO_2 was injected with water versus CO_2 alone. Other

study used glass beads micromodel to study CO_2 injection (Cinar et al., 2009). In this case, the authors positioned their micromodel vertically and used a heptane-rich phase as the nonwetting displacing phase to investigate the effect of gravitational, viscous and capillary forces in a CO_2-like injection. Riazi et al. (2011) studied CO_2 injection for both applications, EOR in depleted oil and gas reservoirs and GCS in saline aquifers. They concluded that supercritical CO_2 has a higher trapped saturation relative to gaseous phase, and showed how solubility trapping can be enhanced when injecting water after CO_2.

Kazemifar et al. (2015) and (2016) published a series of microfluidics experimental studies concerning displacement mechanisms for supercritical CO_2 ($scCO_2$)-brine system in a porous matrix. They used Particle Image Velocimetry (PIV) in their studies to capture interfacial topology and brine velocity fields at pore-scale. Other studies from the same series of experiments were performed by Li et al. (2017) and (2021) (Fig. 3) who used high speed Micro-PIV in their experiments to study flow dynamics at reservoir conditions in engineered porous structures.

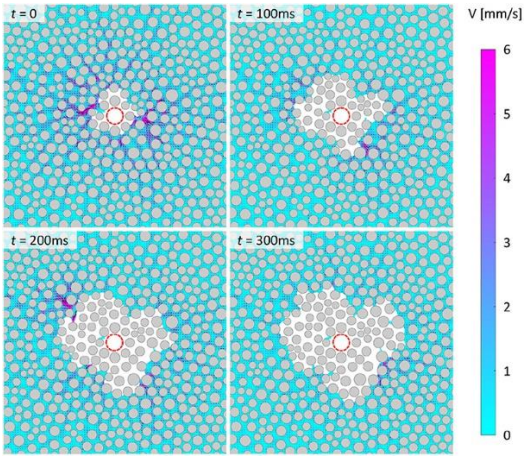

Figure 3: Velocity fields of CO_2 displacing water in a 2D hydrophobic micromodel. (Li et al., 2021).

Research efforts have also been centered on using experiments to validate computational models. Cheng et al. (2018) performed heterogeneous micromodel experiments using a design inspired by a sandstone pore structure. They investigated whether Lattice Boltzmann simulations can reproduce the CO_2 invasion patterns that was observed during the experiments for a range of capillary numbers under reservoir conditions. They found that the simulations represent important qualitative tendencies in the invasion patterns, although, with some differences in secondary pathways due to inertial effects not considered in the simulations.

CO_2 injection has also been explored in the context of enhanced oil recovery. Amarasinghe et al. (2021) performed vertical micromodel experiments at reservoir conditions to understand how CO_2 convective mixing occurs. They observed how oil had the tendency to find the easiest path out the porous system vs the CO_2, which was most likely to end up trapped in dead end pores. Mahdavi et al. (2016) also involved gravity in their experiments to study the effect of carbonated water injection (CWI) on oil recovery, using glass micromodels positioned horizontally and vertically. Mahdavi and James (2020) evaluated the effect of CO_2 injection systems on oil recovery using vertical micromodel (Fig. 4), along with core-flooding experiments and modeling of different CO_2 injection methods such as CWI and CO_2 water alternating gas (CO_2-WAG). They observed advantages of CWI on oil recovery compared to water injection by itself.

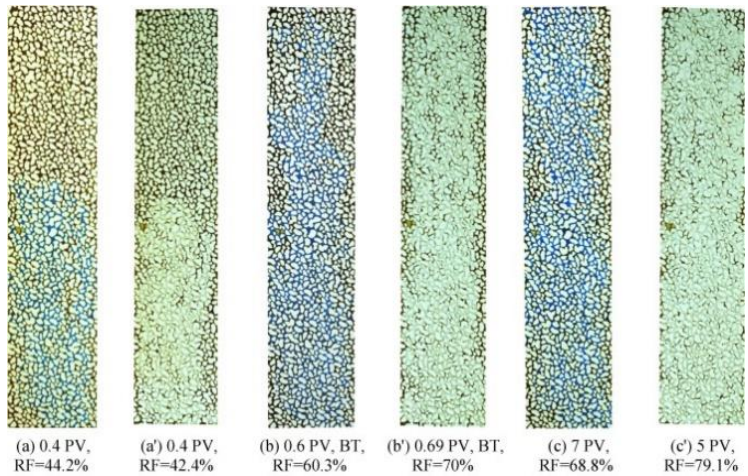

Figure 4: Crude oil Recovery Factor (RF) for vertical micromodel experiments, injecting from bottom to top. Water flooding (a, b, c) and CWI (a′ b′ and c′). (Mahdavi and James, 2020).

Lv et al. (2022) evaluated CO_2 injection in naturally fractured carbonate reservoirs for GCS. They used 2.5D glass micromodels that represented the large and micro-fractures as well as the heterogeneity in porosity present in carbonate rocks. Their glass micromodel was coated with CaCO3 nanocrystals. They observed a higher sweep efficiency and recovery factor percentage when implementing foams with nanoparticles that control CO_2 mobility. Another micromodel application involving injection and storage of CO_2 to improve hydrocarbon production was performed by Jadhawar et al. (2021). They used a micromodel to investigate the concurrent CO_2 storage and methane hydrate gas recovery. They observed the hydrate morphology after injecting CO_2 and captured how the CO_2 molecules replaced methane hydrate previously existing inside the glass micromodel.

2.1.2. Wettability and contact angle measurements.

Wettability influences how fluids interact with rock surfaces. It is defined as the tendency of a fluid to “wet” a surface, and it is typically quantified through the contact

angle, i.e., the angle between a solid and fluid surface. This property is directly linked to the capillary pressure. For example, in more water-wet systems, the capillary pressure, particularly the capillary entry pressure, is lower, leading to easier CO_2 injection. Similarly, the residual saturation of CO_2 is also influenced by the wettability of the rock, as the water-wet rocks are more affine to be saturated with brine. Thus, a better understanding of wettability can help predict the distribution of CO_2 in the subsurface and identify the potential for trapping,

Er et al. (2010) fabricated micromodels with fractures to investigate CO_2-oil interaction and displacement mechanisms during oil recovery. They created homogeneous and heterogenous patterns in glass devices to study the interaction between the matrix and the fracture. They observed how the amount of trapped oil changed with different wettability and miscibility conditions. Fakhari et al. (2018) investigated wettability effects at reservoir conditions when CO_2 invades a water-saturated silicon micromodel. They designed the micromodels based on sandstone X-ray CT scans. They compared the experimental results with Lattice Boltzmann numerical simulations (Fig. 5), finding several pore-scale features captured in both methods.

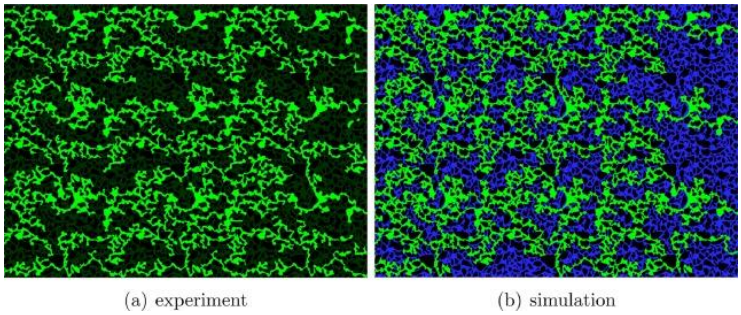

Figure 5: CO_2 final saturation in silicon micromodel vs numerical simulation. (Fakhari et al., 2018).

Other pore-scale experiments involving wettability studies include work by Hu et al. (2017) who analyzed the impact of wettability on $scCO_2$ capillary trapping. They used a homogeneous pattern design on silica-based micromodels and observed that CO_2 trapping increases as the solid shifts to less water-wet (Fig. 6). Kim et al. (2012) investigated how the interactions with $scCO_2$ affected the wettability of silica, the most common mineral in sandstone reservoirs. They used silicon micromodels with a homogeneous pattern where grains were not touching each other. They observed $scCO_2$ can react with the silica mineral very fast, changing the wettability of the surface.

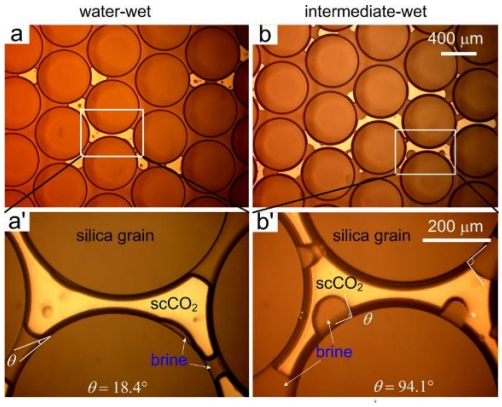

Figure 6: Micromodel experiment results for water-wet system vs intermediate-wet. (Hu et al., 2017).

Jafari et al. (2017) and (2019) measured static and dynamic contact angles in a CO_2-brine system representing reservoir conditions for geologic carbon storage. They fabricated glass micromodels with random patterns and measured contact angles for drainage and imbibition and evaluated the effect of salinity, observing that increased salinity results in increased contact angle measurements for specific conditions.

2.1.3. CO_2 dissolution, diffusivity and exsolution

Dissolution, diffusivity, and exsolution studies can help understand factors such as the temperature and pressure conditions in the reservoir, characteristics of the reservoir rock, composition of the formation fluids and chemical interactions between the CO_2 and minerals. For example, Buchgraber et al. (2012) studied the dissolution of the CO_2 phase during the imbibition of brine and observed different trapping mechanisms depending on the flow rate.

Another salient example is a study by Sell et al. (2012) who presented an experimental methodology to measure on CO_2 diffusivity using micromodels and tested how the CO_2 diffusion coefficient changed with changes in pressure and salinity for GCS applications. They observed that high salinity reservoirs will slow down the diffusion rates and did not detect significant variations when changing pressure. Additional experiment with carbonated water injection (CWI) using microfluidics experiments, include Zuo et al. (2013) who performed CO_2 exsolution studies at reservoir conditions. They fabricated a silicon micromodel representing sedimentary rocks, and injected carbonated water to their model. Then, they depressurized the system to detect the exsolved gas phase. They observed that pore geometry strongly influenced the bubble formation.

In the context of EOR, Lu et al. (2021) studied CO_2 exsolution during huff-n-puff at reservoir conditions. They investigated residual oil and migration mechanisms at different wettability conditions and found that in oil-wet conditions, the aqueous phase blocked throats and formed new pathways causing CO_2 to encapsulate.

2.1.4. Brine dry-out and salt precipitation

Salt precipitation and brine dry-out studies provide insights of geochemical reactions involving dissolved CO_2, brine, and minerals in the formation. Understanding the

mechanisms of salt formation can help develop effective mitigation solutions in porous rocks and contribute to safer and more efficient GCS operations. Furthermore, it can give insights about how the salt precipitation can affect the confinement system and seals, and the ensuing consequences for GCS.

He et al. (2019) fabricated a glass micromodel to study brine dry-out during $scCO_2$ injection which correlates with decrease in injectivity (Fig. 7). They observed how the wettability of the formation influences the distribution and patterns of salt precipitation which has a direct impact on CO_2 injectivity. Other salt precipitation experiments include Miri et al. (2015) who used glass micromodels to study the dynamics of salt precipitation, observing that salt can be massively precipitated inside CO_2 pathways. Nooraiepour et al. (2019) investigated the effects of CO_2 phase state and injection rate in salt precipitation in the shale caprock of a geologic carbon storage project.

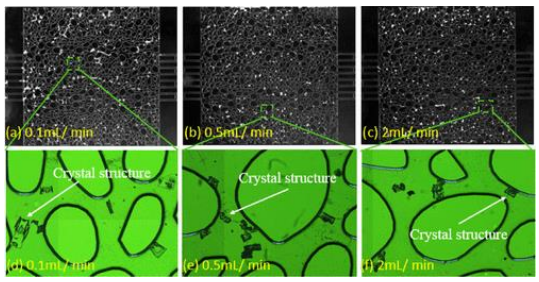

Figure 7: Crystal structures of precipitated salt inside the micromodel for different CO_2 injection rates. (He et al., 2019)

Seo et al. (2019) proposed a methodology to inject sequential water with gaseous CO_2 bubbles to minimize the brine dry-out and accelerate dissolution. They performed experiments with polymer micromodels and observed that sequential injection slows down the brine dry-out compared to continuous injection, and it accelerates the rate of CO_2 hydration in the brine.

Most of the previous studies represent the porous medium as 2D; however, 3D printed micromodels can offer a 3D representation of porous structures. A limitation in this 3D micromodels is their inability to handle high pressure and temperature needed for CGS applications. This challenge can be potentially overcome either by developing new materials in the stereo-photolithography processes or using different fabrication approaches, such as multi-depth glass micromodels.

2.1.5. Real-rock microfluidic studies in GCS

Few microfluidics studies of CO_2 injection have been performed using geomaterials instead of transparent materials (Fig. 8), as summarized in the previous sections. These geomaterials consist of real rock or mineral chips.

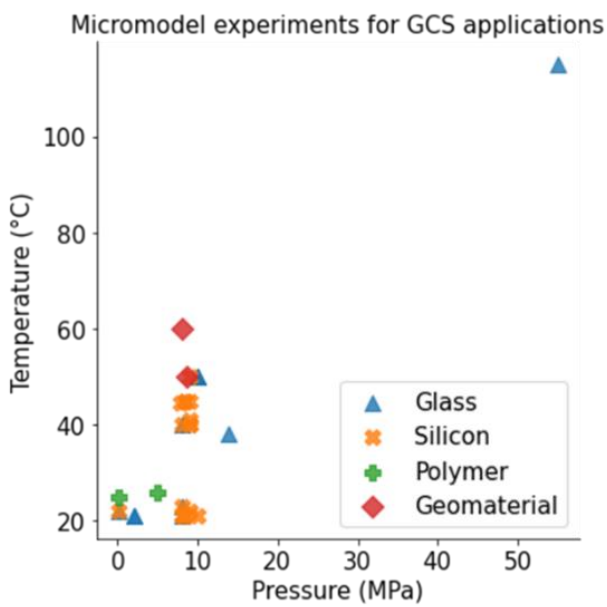

Figure 8: Materials used for micromodel fabrication at different conditions of pressure and temperature.

The studies that used geomaterial include devices created using a shale rock as presented by Porter et al. (2010), who developed a micromodel to investigate injection of $scCO_2$ as non-wetting fluid to displace brine in a shale rock device with fractured patterns (Fig. 9). They imaged a fractured shale rock, and from the obtained micro-tomography images, they created the fracture geometry and laser-etched them in a thick rock slice used as the micromodel. They also studied fracture-matrix interaction with brine imbibition and three phase flow $scCO_2$-brine-oil.

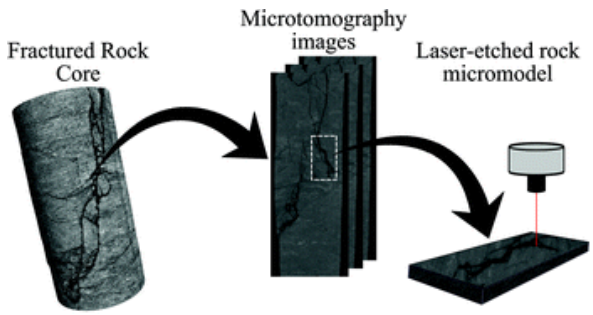

Figure 9: Steps followed for micromodel fabrication using geomaterials to represent fractured rocks. (Porter et al., 2010)

Nooraiepour et al. (2018) also fabricated laser-fractured shale rock micromodels. In this case, they studied the influence of CO_2 phase on salt precipitation. These shale micromodel experiments were performed at reservoir conditions, where the flow occurs through the fractures and allow the system to be pressure sealed.

2.2. MICROMODEL DESIGN AND FABRICATION

2.2.1. Micromodel chip design:

Micro-scale experiments have been developed using microscopic technologies that allow to observe in detail the flow phenomena at the pore-scale, which in turns affects flow processes at larger-scales (Gogoi and Gogoi, 2019). Microfluidics experiments allow to

directly visualize flow through pore-scale micromodel devices and facilitate the study of processes occurring at those scales.

2.1.1.1.Homogeneous patterns:

Homogeneous patterns have a constant porous structure, where the pore body and throat are determined by a recurrent geometry (Fig. 10). Although these constant features are very different from a real structure, these models are very well suited for displacement stability and fluid distribution studies (i.e., Wang et al., 2013 and Zhang et al., 2011).

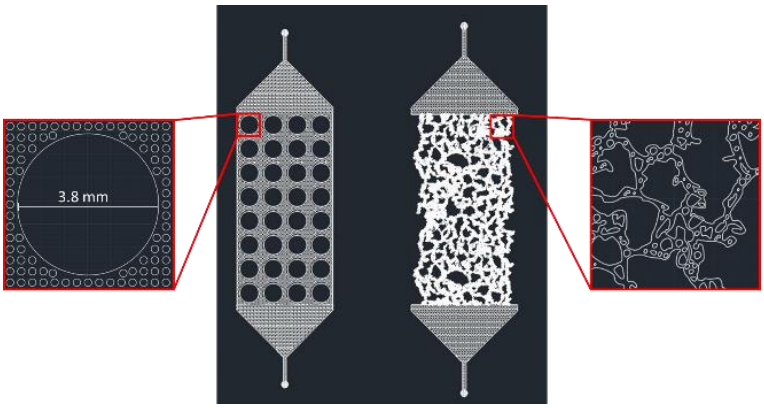

Figure 10: Homogeneous micromodel (left) vs heterogeneous micromodel (right) pattern. The homogeneous micromodel has a grain size of 3.8 mm for the large features.

2.1.1.2. Heterogeneous patterns:

Micromodel designs with a geometric heterogeneous pattern, have geometric features but instead of being constant and recurrent, they can be irregular following a statistical distribution. The shape of the pore body and throat change, and while they do not exactly represent the porous media, they can study phenomena at small-scale. An example of a geometric heterogeneous pattern is presented by Sayegh and Fisher (2008),

who designed a porous medium pattern using a controlled grain algorithm that placed the pore-bodies (grains) in an area, and they controlled size, shape and densities (Fig 11).

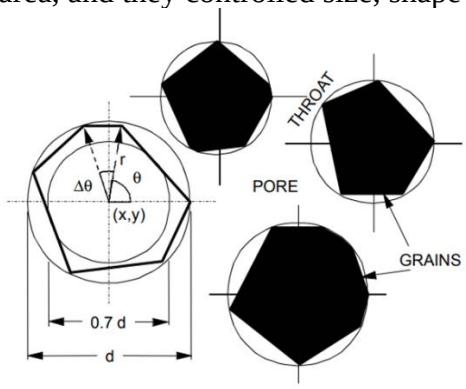

Figure 11: Grains, pore body and pore throat design with a controlled grain algorithm (Sayegh and Fisher, 2008).

Another example of heterogeneous pattern is pore-networks designed to represent porous media. Miri et al. (2015) performed microfluidics experiments to evaluate the dynamics of pore-scale salt precipitation using a pattern with features in a network with a lattice of connected pore bodies that represented the physics of the flow phenomena of an aquifer.

Patterns that aim to replicate a specific pore network (i.e., sandstones, carbonates) can be designed based on images obtained from a thin section of the rock or X-ray computed microtomography (micro CT) image, converted to a binary image of the topological features. Zuo et al. (2013) studied the multiphase flow properties of CO_2 phase in porous media using a micromodel pattern that represented a low permeability sandstone. Fig. 12 shows the process of digitalizing and fabricating a micromodel device from a thin section image from Mount Simon Sandstone (Berger et al., 2019).

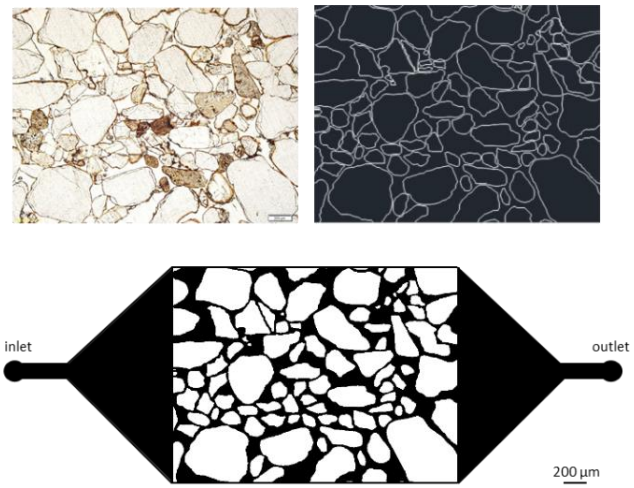

Figure 12: Top left: Thin section image from a Mount Simon Sandstone (Berger et al., 2019). Top right: contour lines of the grains Bottom: Micromodel pattern with black representing pore space and white representing the grains.

2.1.2. Micromodel chip fabrication - materials and methods:

Fluid flow effects in the subsurface are studied using small pores and pore throats represented in the micromodels, therefore, the importance of the resolution of the features during the fabrication process. These features can have 2, 2.5 or 3 dimensions (2D, 2.5D and 3D, respectively). The most common micromodels for porous media studies remain 2D and 2.5D because of their simple fabrication and imaging compared to 3D micromodels (Nuske et al., 2015), although these last ones could be used to evaluate processes more relevant to complex structures. For example, Dimou et al. (2021), created a 3D printed micromodel to study CO_2 dissolution at the pore-scale for CCS applications. The mechanical stability of these 3D micromodels is limited, particularly for supercritical CO_2 operating conditions.

2.1.2.1. Glass and silicon micromodels

Various approaches have been used to fabricate micromodels that allow visualization of fluid flow through a transparent material such as silicon and glass. Some of the first micromodels were fabricated using glass beads spheres between two plates to represent the porous media (Chatenever and Calhoun, 1952). These glass beads micromodels served to demonstrate how transport in small-scale systems affect larger-scale fluid displacement phenomena (Chuoke et al., 1959). Micromodel fabrication using glass beads is a method that is still used for pore-scale investigations. Moebius and Or (2014) fabricated a micromodel device using glass beads to study invasion events during drainage. They located their model vertically and evaluated pressure fluctuations, invaded volume distributions and different geometric pore volume invasions.

Fabrication procedures of micromodels depend on the material. Photolithography is a method commonly used for glass and silicon-based models (Fig. 13). This technique consists in pouring a positive (or negative) photoresist into a previously cleaned substrate and evenly distributing the liquid using a spin coater. Spin parameters such as revolutions per minute (rpm) and total time, control the thickness of the photoresist which will affect the final depth of the pore bodies and throats. The model is then exposed to UV light using a photomask with the pattern desired, if the photoresist is positive, the unexposed areas will be hardened; on the contrary, if it is negative, the exposed areas will harden instead, representing the walls or pore bodies.

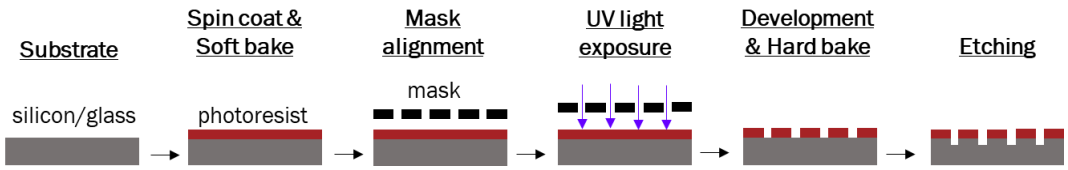

Figure 13: Fabrication protocol of microfluidic devices using photolithography for a positive photoresist.

After this process is finished, the substrate can be etched to reach the depth desired. Fig. 14 shows an image obtained by Scanning Electron Microscopy (SEM) by Buchgraber et al. (2012). They etched the device to reach depths of 25 µm fabricated a silicon micromodel from a carbonate rock image, creating a dual-porosity model where they represented the heterogeneity in porosity.

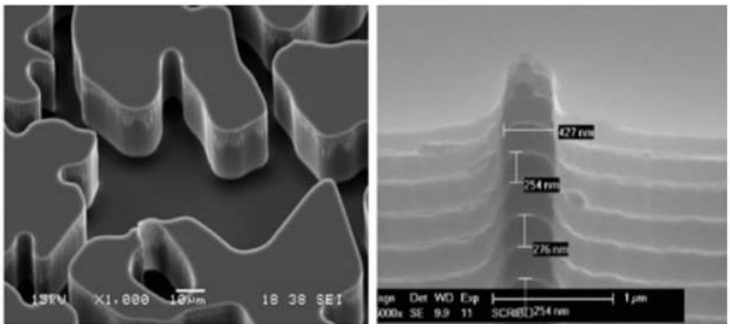

Figure 14: Etched silicon micromodel with channels with an average depth of 25 µm (Buchgraber et al., 2012)

Some advantages of glass micromodels include the low opacity and low cost compared to silicon. However, the wet etching process presents a high chemical hazard in this case. Conversely, silicon-based micromodels are only transparent on one side and require dry etching which is more expensive. Both glass and silicon-based are well suited for high-pressure applications.

2.1.2.2. Polymer micromodels

Soft photolithography is another common fabrication method, it is the preferred technique when using polymeric materials (i.e., polydimethyl siloxane: PDMS or poly-methyl-methacrylate: PMMA). This technique builds a mold using photolithography and the PDMS model is obtained from this mold, thus, multiple models can be fabricated using the same mold. A difference with silicon or glass substrates is that the photoresist usually is negative so that the mold prints the positive pattern in the PDMS. Polymer-based micromodels can be less expensive than silicon-based, have faster fabrication times, and are very transparent. However, they have limitations at high pressure and specific wettability conditions.

2.1.2.3. Real-rock micromodels (RRMM)

Existing techniques for micromodel fabrication using geomaterials mostly include fabrication of devices using shales (as discussed previously) or calcite minerals (Song et al., 2014). with very few studies using sandstone micromodels. This project includes the development of RRMM for GCS applications. There are advantages and disadvantages to using RRMM.

Although micromodels fabricated with geomaterials are not replicable (i.e., geometry patterns), there is still the need to use real rock when interested in chemical interactions between rock and fluids or when interested in maintaining the original wettability of the system. Experience with rock micromodels such as shale has been presented, nevertheless, there is a lack of experiments involving other types of rock such as sandstone or carbonates. When fabricating micromodels with engineered materials, experimental procedures are well developed and allow for faster manufacturing. In contrast to this, RRMM do not have established fabrication protocols. Furthermore, the use of

sandstone micromodels poses a challenge because of the integrity of the rock, compared to more consolidated and less permeable samples (i.e., shale rocks or calcite mineral).

The visualization of fluid flow through RRMM and 3D micromodels is strongly affected by spherical aberration and requires a very careful procedure in order to obtain appropriate and representative 3D data. Previous studies have used Confocal Laser Scanning Microscopy (CLSM) to image 3D micromodels and pore space (Hassan et al., 2021). This technique uses a laser at a given wavelength to excite a fluorescent sample, the laser travels along the axial axis of the sample, obtaining images at various focal distances to acquire a final 3D high-resolution image (Diaspro et al., 2002). Although this imaging technique has not being used during injection and fluid flow tests, it has proven to be a reliable tool when characterizing the three dimensional pore space.

2.3. PROJECT DESCRIPTION

This project is a part of the Gulf of Mexico Partnership for Carbon Capture and Offshore Geologic Storage (GOMCARB). This Partnership encourages the safe, long-term and economically viable storage of CO_2 offshore in the Gulf of Mexico (Fig. 15).

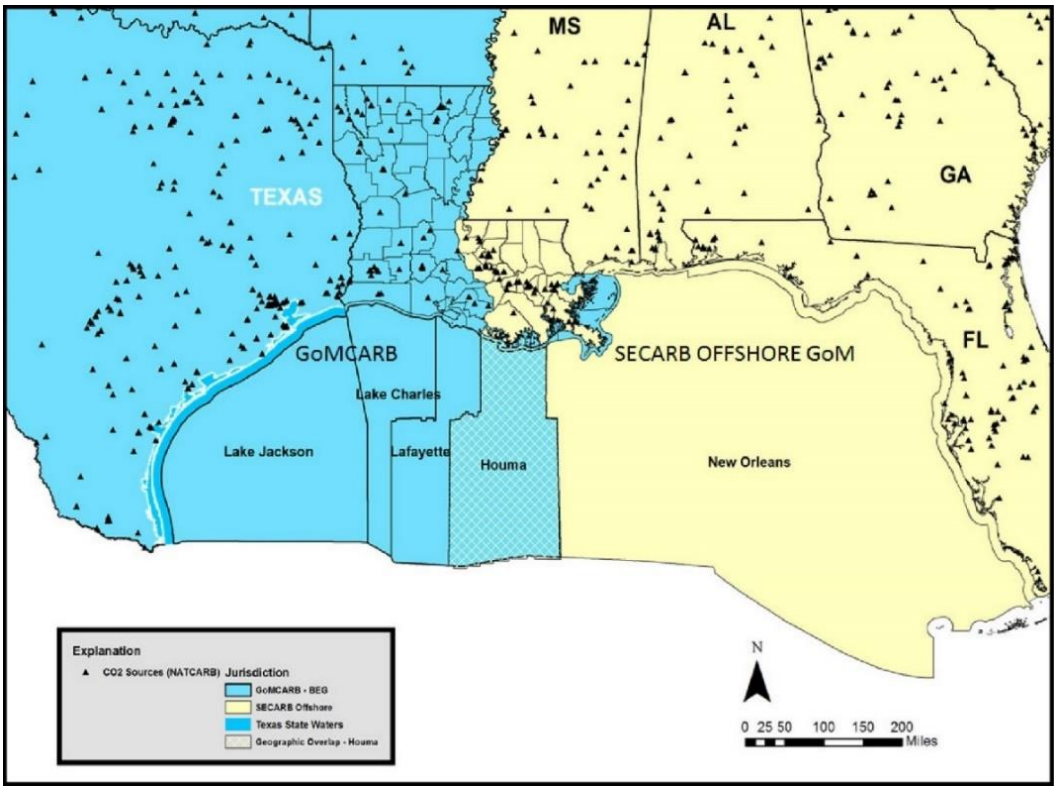

Figure 15: In blue: GOMCARB study region to assess possible CO_2 storage sites in the Gulf of Mexico in the Texas and Western Louisiana coast (GCCC, 2023).

The purpose of this study is to investigate capillary pressure curves at different capillary numbers during drainage process, for various sandstone micromodels. Capillary pressure curves are currently obtained experimentally through core-flooding or using pore-scale modeling. Currently, no established method exists for measuring capillary pressure during gas/water imbibition, thus, Lun et al., (2023) recommend not using capillary pressure curves obtained from imbibition process (Likanapaisal et al., 2023). The capillary pressure curves obtained in this study will provide a new insight when matching the microfluidics experimental results with modeled capillary pressure values. Fig. 16 summarizes the processes involved for every step in chronological order.

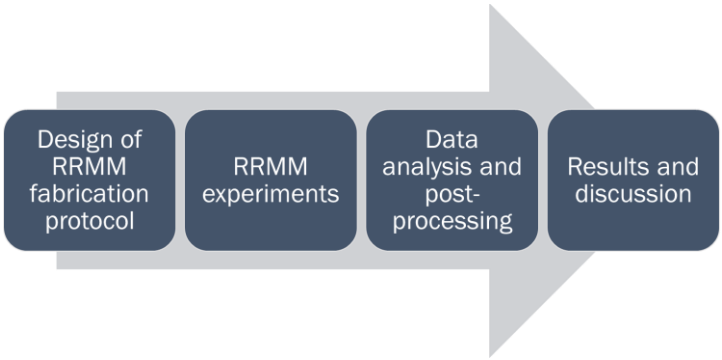

Figure 16: Research plan used in this thesis organized in chronological order.

Chapter 3: Real-rock Micromodel Fabrication Protocol

3.1. DESIGN OF A FABRICATION PROTOCOL TO BUILD RRMM:

To accomplish the successful fabrication of sandstone micromodels, numerous approaches were involved. The main restriction of designing RRMM is to create a device that can stand high pressure and high temperature (HPHT) to be able to inject $scCO_2$. Transparent engineered materials such as silicon, glass, polymers, and 3D printed structures are commonly used to fabricate microfluidics devices. However, a significant limitation of such materials is that they partially represent the porous structure of rocks but are unable to capture the real rock-fluid interaction.

As discussed earlier, only a few studies have been performed using real rocks due to challenges during the fabrication process, such as repeatability, which leads to not having careful control of reservoir properties (e.g., porosity, grain/pore size). The majority of the fabrication protocols using real rock micromodels have been developed for shales and minerals such as calcite. In this project, I present the challenges and advances in developing a fabrication technique that involves sandstone micromodels.

Initially, different fabrication methodologies were tested, and each technique presented advantages and limitations (Table 2). The first two methodologies using glass and glass-epoxy devices had sealing problems between the top and bottom layers with the thin section. Flow was preferentially at the top/bottom layer – thin section interface, rather than through the porous thin section.

The grain-packed model improved the imaging and allowed the fluid interface to be visualized when using homogeneous grain sizes. However, this technique has challenges related to finding sandstones with homogeneous grain shapes, biasing the flow processes

towards homogeneous samples. Furthermore, grain disaggregation alters the structure and cementation of the rock.

The objective of this thesis is to use a micromodel that represents the rock as realistically as possible. Therefore, I chose the fabrication approach involving PDMS and thin sections. Although this methodology does not have the resolution needed to observe fluid interfaces between two fluids, it allows us to see the overall distribution of dyed fluids and make saturation estimates using the volume of fluid injected. Furthermore, this technique allows to measure pressure during the injection process. If successful, different fluid-rock interaction studies could follow, such as, salt precipitation and brine dry-out studies.

Device	Advantages	Limitations
Glass	- Could stand HPHT	- Sealing between the rock surface and the glass.
Glass-epoxy	- Could stand HPHT	- Sealing between the rock surface and the glass or epoxy.
Grain-packed	- Could stand HPHT - Existing fabrication procedures from literature that used glass beads - Good imaging	- Cementation is destroyed when the grains are separated.
PDMS - Thin section	- Existing fabrication procedure from literature - Imaging allows to see injection of dyed fluids. - Sealing and bonding using PDMS.	- Does not stand HPHT. - Gas injection could be affected due to PDMS being permeable to gases. - Size of the device is larger because of the thin section.

Table 2: Advantages and limitations of fabricated micromodel devices

There is no previous evidence of studies using sandstone micromodels specifically for CO_2 injection into saline aquifers. Nevertheless, Singh et al. (2017) created a sandstone fabrication protocol to study two phase flow inside a real rock micromodel. An important limitation of their methodology is ambient conditions (temperature and pressure). However, given the previous non-successful attempts to fabricate a HPHT device, this

project will modify their technique for geological carbon storage applications. Fig. 17, shows the steps followed to fabricate the PDMS RRMM.

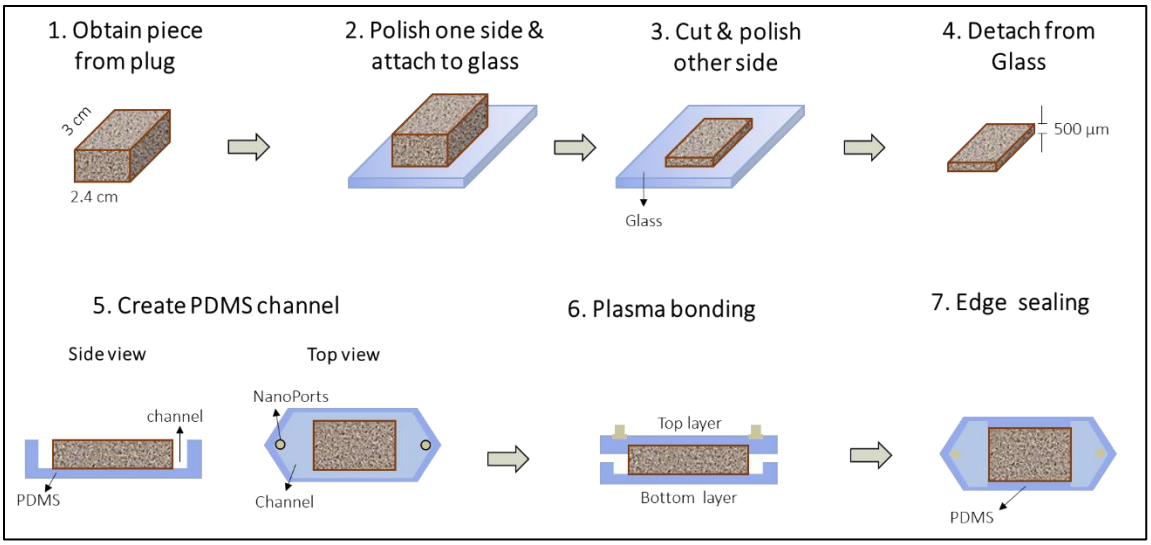

Figure 17: Real-rock micromodel fabrication procedure

(1) First, I need to obtain a slice of rock from the rock plug. (2) Then, polish one side of the thin section until smooth, and adhere the polished side to a glass slice using a strong adhesive (e.g, Superglue). (3) Cut the rock piece and polish the second surface of the thin section (4) Detach the glass from the thin section (5) Pour liquid PDMS in a mold to create a channel in which the fluids will move. (6) Bond the rock to the PDMS and the two PDMS layers together. (7) Seal the edges to allow the injected fluids to move only through the rock slice to allow injection of liquid PDMS in the channel. It is necessary to punch multiple holes along the edges of the model prior to the plasma bonding.

3.2. THIN SECTION FABRICATION

I use a sandstone rock slice as our porous system, in which fluids will flow through. This slice has to be “thick” to maintain the mechanical integrity of the thin section, but also

thin enough that allows imaging of the fluorescent dyed-fluid and interpretation of the saturation from a 2D image. The proposed thickness is around 500 µm based on previous literature and our own experience using Berea and Lower Tuscaloosa sandstone from CFU Well # 31-F3 at a depth of 10,447 ft (Hosseini et al., 2013). After obtaining the core plugs, these are cut into cubes of 24x30 mm using a diamond saw. The rock piece is ground using Hillquist grinder machine (located at JJ Pickle Research Campus), and then polished until smooth. When one of the sides is smooth (Fig. 18A), the rock piece is placed in a Thelco Oven (located at Pickle Campus) at a temperature of 105°C overnight, to make sure all water is removed from the rock.

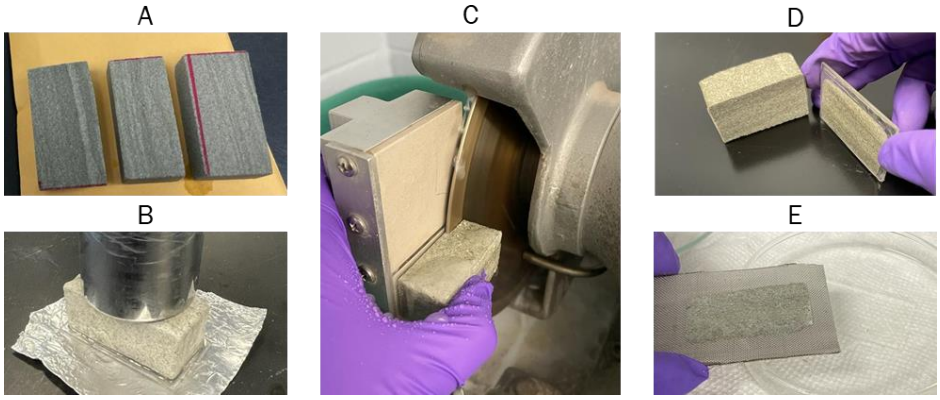

Figure 18: Step by step of a slice section fabrication of a sandstone rock. A) Side 1 polished. B) Attached the polished side to a glass slice and applied weight. C) Cut sample into a rock slice. D) Thin section after grinding. E) Final thin section after being polished and detached from glass.

After the samples are dried, a layer of Superglue is carefully spread throughout the smooth surface of the rock, until it has impregnated around 1mm of depth. The rock is placed under vacuum for around 15 min to avoid air bubbles trapped. A glass slice is then attached to the smooth surface and a weight is placed on top of the sample overnight (Fig. 18B). The sample is then cut into a 1-2 mm thick rock slice (still attached to the glass slice)

using the Hillquist diamond saw thin section machine (Fig. 18C). To smoothen the surface, the Hillquist grinder machine is used (Fig. 18D), the sample is washed with distilled water and allowed to dry at room temperature. Then, the exposed surface is manually polished until smooth using an established polishing procedure (Table 3).

Step	**1**	**2**	**3**	**4**
Abrasive Size	120 grit	220 grit	320 grit	1000 grit
Brand	3M	3M	3M	3M
Lubricant	None	None	None	None/water
Time	5-30 min	5-30 min	5-30 min	5-10 min

Table 3: Polishing procedure for thick section fabrication

After the thick section is polished, it is soaked in acetone overnight (from 12 to 16 hours) to de-attach from the glass. After this time has passed, it is washed in acetone from 3 to 5 more times and then washed using distilled water until the rock is free of acetone and Superglue. Acetone alters the wettability of the quartz when exposed to long times (>2 days), (Al-Yaseri et al., 2022). However, I anticipate this effect to be small as the acetone used to remove the Superglue was in contact at most for one night. The final rock slice is optically inspected (Fig. 18E).

3.3. PDMS PROCEDURE

The RRMM will be fabricated combining thin section fabrication methodologies with soft photolithography techniques. Soft photolithography is a common fabrication method that uses polymeric materials, for this particular case, the soft polymer is Polydimethylsiloxane (PDMS).

Polymer-based micromodels can be less expensive than silicon-based and have a faster fabrication time when using the same mold to fabricate multiple models. PDMS is a

very common material, and its transparency is an advantage for studies that include optical systems. PDMS will be used to fabricate the top and bottom layer of the model, and its soft texture after cured helps maintain the integrity of the sandstone and seal the top and bottom part of the thin section.

3.3.1. PDMS layers and channel pattern

The top layer is fabricated using Sylgard-184® Silicone Elastomer base and curing agent (Dow Corning) with a weight ratio of 10:1: for every 30 g of PDMS elastomer solvent, I added 3 g of hardener. After stirring both parts, the mixture is introduced inside the vacuum chamber to degas it for 20-30 min until no air bubbles remain. After the Nano Ports are placed in the mold, the mixture is poured and the final thickness of the layer is around 2 mm (Fig. 19A). The setup is placed in the oven at 70° C for 2 hours to allow it to cure completely (Fig. 19B). Then, multiple holes are punched along each side of the main channel in regular intervals, using a 1/16-inch puncher (Fig. 19C). The process for the bottom layer is similar, however it does not include the channel.

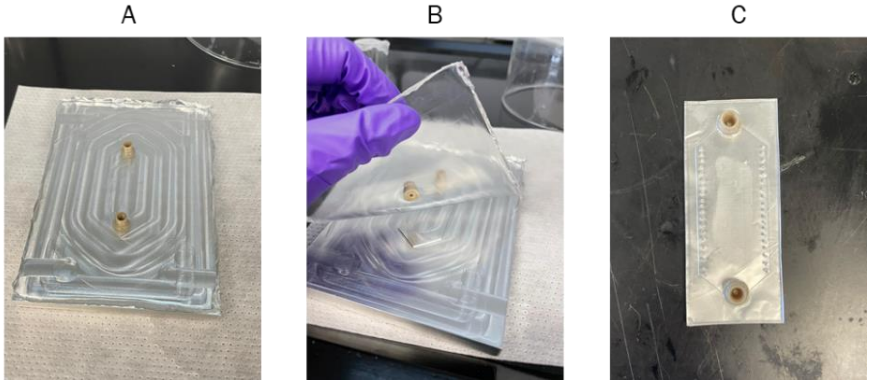

Figure 19: A) Top PDMS layer. B) Top PDMS layer being removed from mold with channel and Nano Ports on it. C) Top PDMS layer with punched holes on the edges.

3.3.2. PDMS plasma-activated bonding

Oxygen plasma bonding was used to bond the PDMS substrates with the thin section and then bond the two substrates together. Bonding PDMS to a polished sandstone surface can be challenging due to the roughness of the polished thin section. The surface roughness plays an important role in determining the strength and durability of the bond between PDMS and the rock slice. The polishing procedure developed allowed for a glass-mirrored finish which helped improve the adhesion of the PDMS to the substrate.

To achieve the bonding, the Asher Nordson March PX-250 from the Microelectronics Research Center (MRC) Cleanroom was used. The plasma-activated bonding works by introducing the samples inside the plasma cleaner (bonding surface pointing up). This procedure removes contamination from the surface of the samples and activates the PDMS surface (Fig. 20), and allows bonding with either rock, glass or another piece of PDMS treated (Duffy et al., 1998). This bonding procedure was designed using trial and error experiments. The optimal bonding operating conditions include, oxygen as gas, and a processing time of 45 seconds each as recommended by Singh et al. (2017).

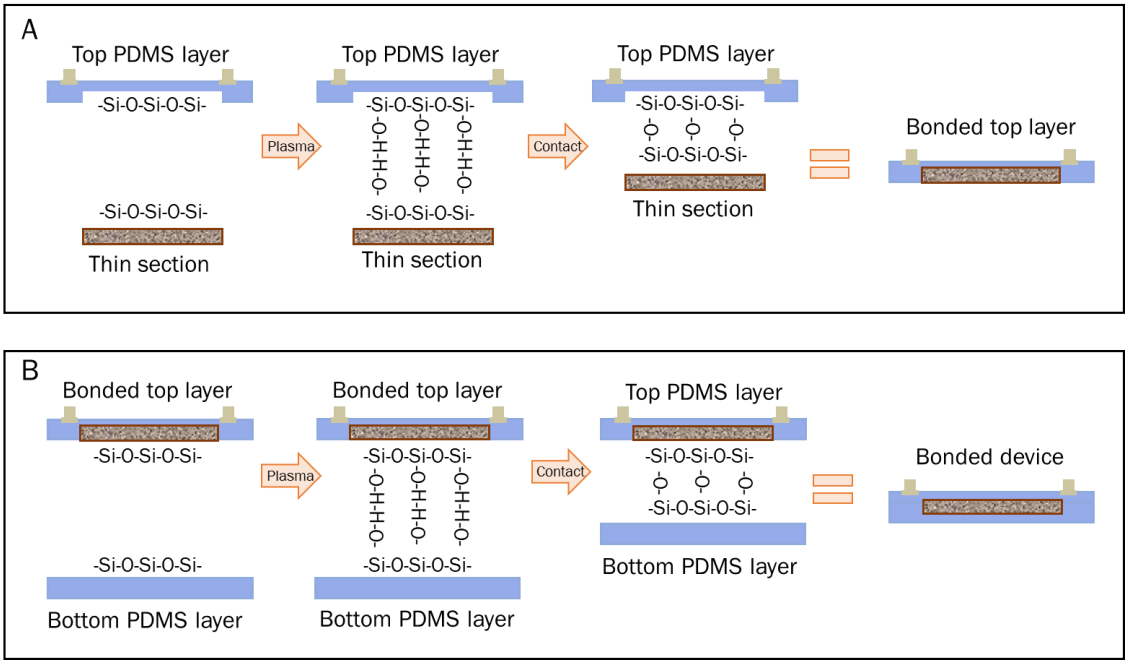

Figure 20: Plasma-activated bonding scheme between two PDMS layers and thin section. A) Bonding between one surface of the rock and top PDMS layer. B) Bonding between second surface of the rock and bottom PDMS layer.

Initially, the bonding was not uniform and some parts of the model were left without a strong bond (Fig. 21). Thus, the same bonding process was compared using two different PDMS layers: a PDMS-coated glass with 500 µm thickness and a PDMS layer with 2 mm thickness. Results obtained from this experiment show a uniform bonding between the two PDMS layers and non-uniform bonding between the top layer and the PDMS-coated glass. The thicker bottom layer also improves the sealing of the device after bonding. This occurs because of the soft layer between the plexiglass and the rock slice when the pressure is applied. In conclusion, a bottom layer of 2 mm was selected instead of the 500µm PDMS-coated glass.

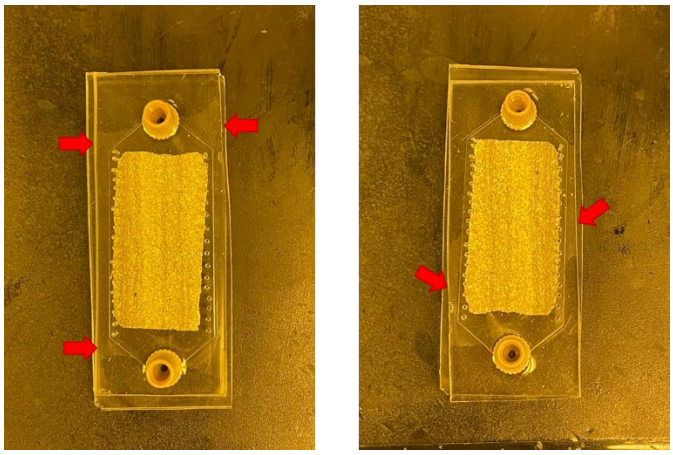

Figure 21: Not-bonded spots on device after bonding process using a PDMS-coated glass with 500 µm thickness.

The plasma activation needs to be done twice in order to bond the device on both sides. During the first run, the top face of the thin section and the top PDMS layer are exposed to plasma (Fig. 22A). Then, during the second run, the bottom face of bonded thin section and the bottom PDMS layer are exposed. The oxidized surfaces are brought into contact and slightly pressed together for 30 seconds. Immediately after the contact, the bonded device (Fig. 22B) is taken to a hot plate at 100°C for 60 seconds to strengthen the bonding.

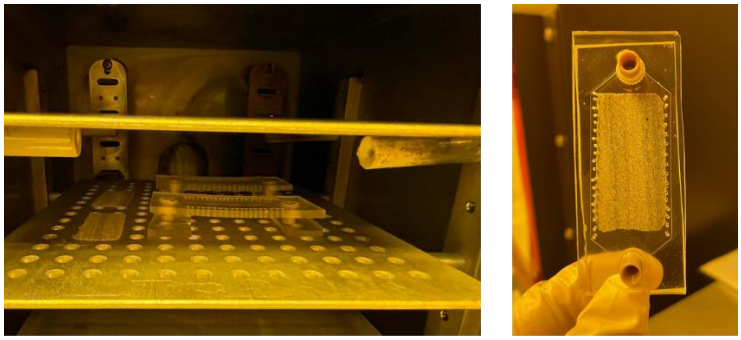

A B

Figure 22: A) Top face of the thin section and bottom PDMS layer exposed. B) Bonded device.

Some additional observations for this process include the exposure time which should not be higher than 2 minutes total, as this can atrophy the exposed surface of the PDMS and decrease the quality of the results. The selected 45 second exposure was carefully evaluated. Note the top layer is exposed twice (90 seconds), however this total time does not affect the quality of the bonding. The additional step of bringing the model to a hot plate at 100°C for 60 seconds provides additional bonding from the high temperature, improving the bonding strength. Another observation is related to pressing together the samples. Pressing with excessive force or while moving or pulling the surface could affect the model and its bonding integrity.

3.3.3. Edge Sealing

After the bonding process is finished, the remaining empty space on the edges of the rock is filled with PDMS. To do so, the bonded device is placed on top of a hot plate at 100°C and the liquid PDMS (previously degassed) is slowly injected through the punched holes towards the channel (Fig. 23A). The PDMS will invade the rock causing to have non-uniform edges on the thick section. The high temperature while conducting this procedure expedites the curing of the PDMS and minimizes the PDMS invasion into the micromodel. Furthermore, applying excessive PDMS can cause the top layer to lift and affect the bonding between the PDMS and the rock.

The final assembly of the micromodel device consists in adding two transparent polycarbonate sheets (of around 2.4 mm thickness) on the top and bottom of the model and then pressing the two layers using screw-compressor clamps around the border (Fig. 23B).

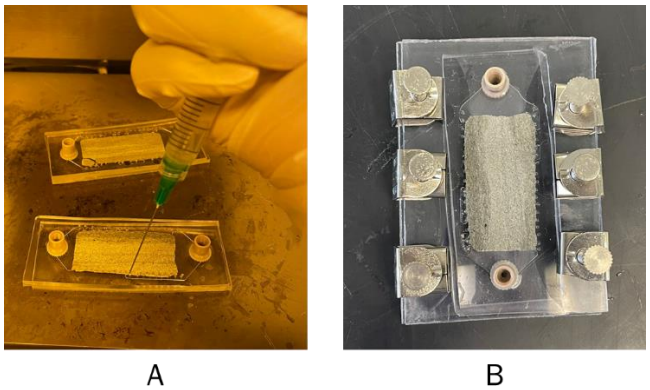

Figure 23: A) Liquid PDMS injected to fill up the channel on the edges of the thick section. B) Assembled device.

Chapter 4: Experimental Materials and Procedure

4.1. BEREA SANDSTONE AND LOWER TUSCALOOSA FORMATION

4.1.1. Berea Sandstone

Berea sandstone is a common rock used for core-flood experiments due to its uniform and consistent porosity and permeability (Churcher et al, 1991). I obtained this sample from a commercial vendor (Kocurek Industries, Inc). This sandstone rock has been extensively studied and the results from fluid flow experimental work are well-documented (Krevor et al. 2012). The Berea samples used in this thesis were characterized by its homogeneous layers with a porosity of 20% (porosity value obtained from vendor), and the fluids were injected parallel to the bedding layers, nearly imperceptible to the eye (Fig 24, Left).

4.1.2. Lower Tuscaloosa Sandstone

The second type of sandstone used in this thesis is from the Cranfield Field Unit (CFU), specifically, the Lower Tuscaloosa sandstone reservoir, where CO_2 has been previously injected as part of a CO_2-EOR pilot project. The Cranfield injection site is simple domal structure located ~20 km east of Natchez in Adams and Franklin County, southwest Mississippi, U.S.A (Lu et al. 2012). This rock is characterized by significant heterogeneity in the porosity and grain size distribution (Krevor et al., 2012). The samples were obtained from the Core Repository at the Bureau of Economic Geology, well # 31-F3. The depth of my sample is 10,447 ft, where there is presence of cross-laminated mud layers (Fig. 24, Right). The porosity of the sample is 18.33%. This porosity value was previously obtained from conventional plug analysis publicly accessible as part of the

SECARB Project. Previous work by Kordi (2013) described in detail the Tuscaloosa samples at the depths of interest.

4.1.3. Relevance of materials tested for CO_2 microfluidic studies.

The two rock types tested cover a range of rock types. Understanding of the capillary pressure response is critical especially for injection of CO_2 into closed-boundary formations. During CO_2 injection in highly heterogeneous formations, the CO_2 plume interaction with these high and low porosity and permeability facies can impact pressure build-up. To analyze this process, core-flooding experiments are typically used; however, they are often time consuming, expensive, and non-repeatable (Krevor et al., 2012, Bakhshian et al., 2020). Obtaining capillary pressure curves using real rock micromodels helps the understanding of the pressure response at a lower cost and faster interest.

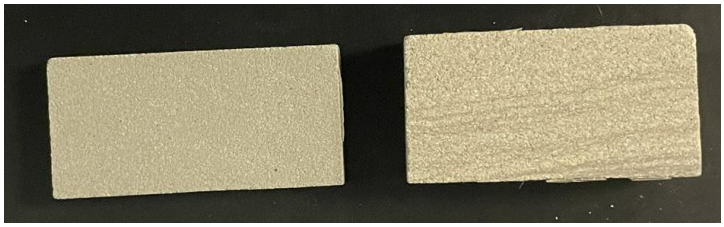

Figure 24: Left: Berea sample. Right: Tuscaloosa sample at 10,447 ft with presence of cross-laminated mud layers.

4.2. FLUIDS

Since our experimental setup is at atmospheric conditions and the CO_2 injection in the subsurface takes place at reservoir conditions (HPHT), I will use analogue fluids to be able to represent supercritical CO_2 injected in a brine-saturated system. A mixture of 50:50 w/w glycerol-water will represent the wetting fluid (brine) and n-heptane pure will represent the non-wetting fluid (CO_2). These analogue fluids were selected based on a

previous study by Krishnamurthy et al. (2022) where they used them to study supercritical CO_2 injection in a sand tank. Both heptane and the glycerol-water mixture are chemically stable and relatively safe to handle, making them convenient analogues for supercritical CO_2 and brine in micromodel experiments. The selection of these fluids was based on their capacity to simulate the capillary-dominated displacement of supercritical CO_2 in the system (Krishnamurthy et al., 2022) and their physical properties that represent those of the CO_2 and brine in the subsurface, such as viscosity ratio (Espinoza and Santamarina, 2010). Table 4 summaries the fluid properties measured by Krishnamurthy et al. (2022).

The glycerol-water mixture was dyed with Fluorescein to allow the fluid to be captured with fluorescent microscopy and the n-heptane was dyed with Oil red O to facilitate the imaging by highlighting the contrast between the two fluids.

Step	**Density (kg/m3)**	**Viscosity (cP) @ 22°C**
Glycerol-water 50:50 w/w	1,115.4	6.25
n-Heptane pure	684	0.41
Interfacial Tension	0.036 N/m	

Table 4: Analogue fluid properties from selected wetting and non-wetting fluids (Krishnamurthy et al., 2022).

4.3. EXPERIMENTAL SETUP AND PROCEDURE

The flow tests setup includes: (1) fluid injection system, (2) imaging equipment, and (3) micromodel devices (Fig. 25). The injection system includes the Harvard Standard Syringe Infusion Pump 11 Elite, which is used to inject dyed glycerol-water mixture and n-heptane into the micromodel, the Teledyne ISCO D-Series pump is used to inject CO_2 to

remove air from the system and the Edwards Vacuum Pump to ensure there is no air trapped in the model. The wetting fluid is detected using the water-soluble fluorescein disodium salt as a fluorescent dye. The imagining equipment involves the Zeiss Stemi 508 Stereo Microscope using the AxioCam 305 and the NightSea Fluorescence Adapter, which allows the visualization of the dyed fluid in the wavelengths range of 450-490 nm. Two pressure transducers were set, one between the inlet and the pumps, and the second one between the outlet and the discharge vessel. These pressure sensors give information about the pressure drop in the micromodel during the flow injection.

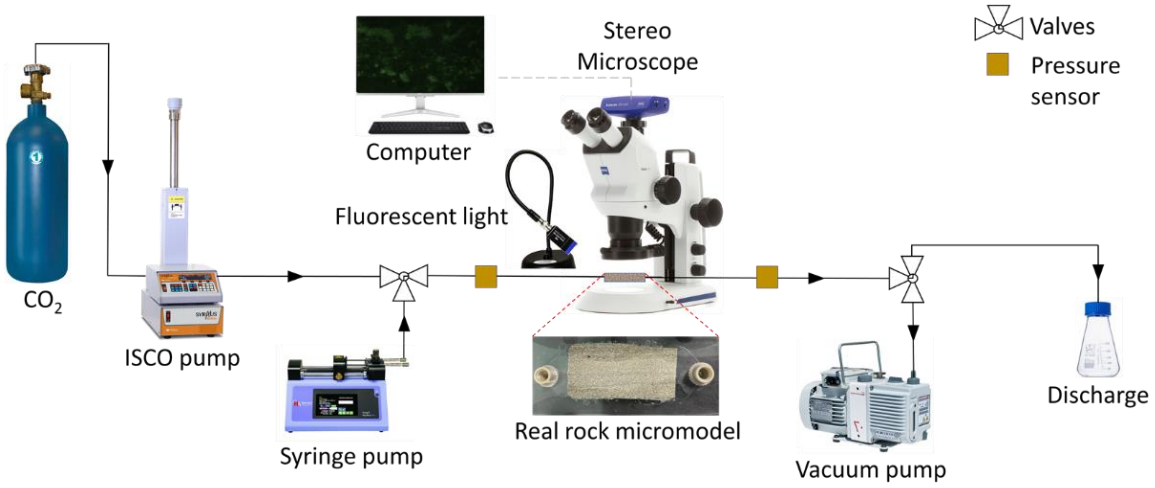

Figure 25: Scheme of experimental setup showing injection system, imaging equipment and micromodel device.

After the micromodel was completely assembled, a combination of injection of gaseous CO_2 with vacuum ensured no air was trapped in the system. After this, the dyed wetting phase (green) was injected for at least 10 porous volumes (PVs) to saturate the model. Then, the non-wetting phase, dyed red (heptane), was injected into the micromodel to replicate a drainage process at a constant flow rate. The experiments were conducted at

~22°C and atmospheric pressure. To achieve different capillary numbers (Ca) (i.e., 6.70×10^{-6} to 7.98×10^{-7}), the injection rates were changed for each experiment. During each experiment, a sequence of images was taken at different time intervals associated with specific saturation points. These images were then analyzed to determine the pixel intensity to approximate fluid saturation.

Chapter 5: Fluid Flow Experiments in Sandstone Micromodels

This chapter presents the two-phase flow experimental results using sandstone micromodel devices. First, the procedure for saturation estimates based on the images is presented. Then, pressure measurements are used to derive capillary pressure versus saturation curves. A range of injection rates and capillary numbers are explored to investigate capillary pressure behavior and residual saturations.

5.1. PORE VOLUME AND CAPILLARY NUMBER

The pore volume (PV) was calculated using equation (5.1), where A_m is the area of the micromodel, T_m is the thickness of the thin section, and ø the measured porosity. The area was measured using the FIJI ImageJ software (Schindelin et al., 2012) on the initial image of the sample.

$$PV = A_m * T_m * \text{ø} \tag{5.1}$$

First, I convert image pixels to mm using a known scale in the image. Then, the pore space area A_m was selected by considering only the pore space available for flow (Fig. 26, lighter area) and discarding any area invaded by the PDMS (Fig. 26, darker area). This area measurement (Fig 26, area inside yellow lines) was repeated 5 times to obtain an average. The thickness of the micromodel T_m was obtained by subtracting the thickness of the Superglue ~370 µm to the measured thin section thickness, measured with a caliper. The porosity of the samples is described in section 4.1, Berea sandstone $\text{ø} = 20\%$, and Tuscaloosa sandstone $\text{ø} = 18.33\%$.

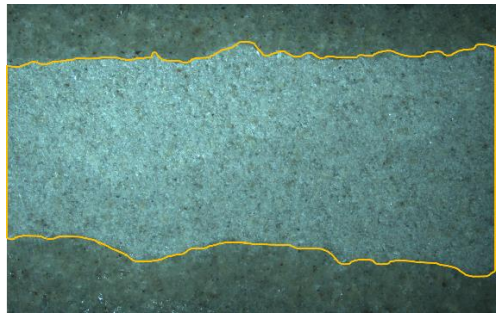

Figure 26: Example of area selection for PV calculation using ImageJ. The lighter area inside the yellow lines is the dry rock sample (before injection), and the darker area is the PDMS bonded edges.

The capillary number quantifies the relationship between viscous and capillary forces in a porous medium. This number was calculated using equation (5.2), where μ_{fl} is the viscosity of the heptane (invading fluid), υ_{inlet} is the flow velocity at the inlet and σ the interfacial tension between the water-glycerol mixture and heptane. The velocity at the inlet corresponds to a "pore velocity", where velocity is calculated by dividing the flowrate (µL/min) with the transverse area for flow (width*thickness*porosity) of the micromodel. Every fabricated micromodel varies in width; thus, the Ca varies slightly in each case.

$$Ca = \frac{\mu_{fl} * \upsilon_{inlet}}{\sigma} \tag{5.2}$$

Table 5 shows the capillary numbers calculated for a flowrate of 50 µL/min for the Berea sample and flow rates of 5 and 50 µL/min for Tuscaloosa samples.

Micromodel #	**Sample**	**Flow rate (µL/min)**	**Ca**
1	Berea	50	6.70×10^{-6}
2	Tuscaloosa	50	8.36×10^{-6}
3	Tuscaloosa	5	7.98×10^{-7}

Table 5: Capillary number for each sample used during the experiments at specific flow rates.

Lenormand et al., 1988, used a phase diagram chart to predict the boundaries of different types of displacement patterns during immiscible fluid displacement in porous media, including viscous, stable, and capillary flow regime. Fig. 27 displays the flow regime boundaries as a function of the logarithm of the viscosity ratio (logM) and the logarithm of the capillary number (logCa) (Yiotis et al., 2021). The occurrence of these displacement regimes depends on multiple factors, such as flow conditions, fluid properties and geometry of the system. As the injected CO_2 migrates away from the injection well and the CO_2 plume spreads out, its velocity decreases. As a result, capillary forces become dominant, promoting capillary-dominated flow regimes. Our experiments were performed using a LogM= - 1.18 and the capillary numbers previously reported.

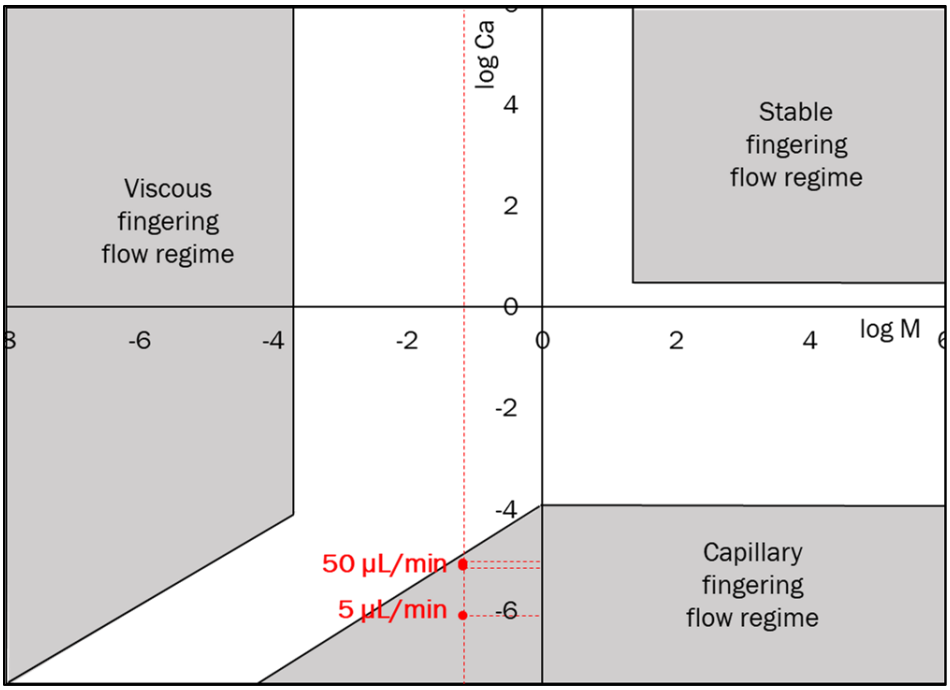

Figure 27: Boundaries for viscous, stable, and capillary flow regimes proposed by Lenormand et al., 1988. Red dots show our experiments inside the capillary fingering flow regime.

5.2. SATURATION ESTIMATION ANALYSIS

The pixel intensity in the microscopy images combines information of the materials and fluids present. Then, changes in pixel intensity can be approximated to fluid saturation during the flow tests. In our system, the saturation represents the fraction of the pore space that is filled with the receding fluid. This fluid is identified in the images using fluorescent microscopy (Fig. 28). However, this procedure does not consider pixels within each pore; the pixel resolution exceeds the pore size and the obtained 2D images are averages across the micromodel thickness. Instead, I consider changes in intensity during the flow test as proxies for fluid saturation within the pixel.

For example, in the wetting phase injection sequence, when the model was completely saturated with the wetting fluid, the pixel intensities correspond to a wetting fluid saturation of $S_w = 1.0$ (Fig. 28, top right). The decrease in wetting fluid saturation as the non-wetting fluid is injected is then calculated by quantifying the decrease in intensity between a given time-step and the initial image (100% wetting phase) (Fig. 28, bottom).

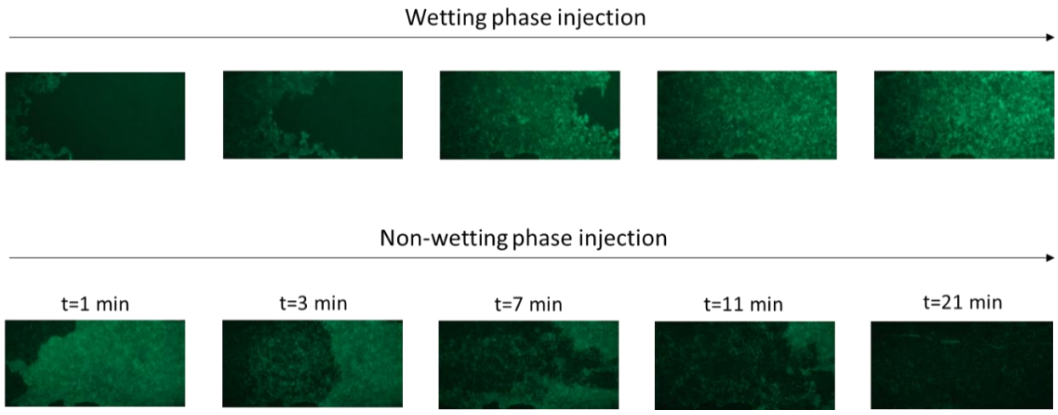

Figure 28: Example of typical optical microscopy images acquired during injection. *Top row*: The sample was dry and wetting fluid (green) injection started from left to right. *Bottom row*: The sample was saturated with wetting fluid (green) and non-wetting fluid (black) starting from left to right. Time increases from left to right.

To calculate the wetting fluid saturation, the images were initially processed using ImageJ and the intensity of the pixels analyzed using MATLAB. First, the images were separated by splitting the image color channels (red, blue, green) and finding the channel that offers the best contrast between the fluids. In this case, the green channel was used. Then, the images were cropped to the area of interest and exported. Following this, the "green" intensity was obtained for each pixel and averaged over the entire micromodel to obtain a global saturation value in each time step.

The saturation of the wetting fluid (S_w) is calculated using the information acquired before injection when saturation of wetting fluid is zero ($S_w = 0$) and after the wetting fluid injection is finished, when the saturation of wetting fluid is 100% (S_w=1):

$$S_w = \frac{I_{ex} - I_w^{sat}}{I_{nw}^{sat} - I_w^{sat}},\ S_{nw} = 1 - S_w, \tag{5.3}$$

where I_w^{sat} and I_{nw}^{sat} are the intensities when the sample was saturated with wetting and non-wetting fluid respectively, and I_{ex} the is the current intensity of an image obtained from a partially saturated sample during the experiment. This procedure is repeated for every time step.

5.3. PRESSURE MEASUREMENTS ACROSS THE MICROMODEL

The total pressure drop across the micromodel (ΔP) was recorded using two LabSmith uPS pressure sensors, located, one at the inlet and one at the outlet line of the device. The pressure was constantly measured throughout the duration of the flow experiment taking around 2 - 4 measurements per minute.

Konangi et al, (2021) presents Eq. 5.4, where the pressure drop between the inlet and outlet (ΔP) is compared to the macroscopic capillary pressure $P_c(S^w)$. They emphasize

how this relationship is valid when pressure remains constant within each phase. The macroscopic pressure definition (Eq. 5.4) is applicable in equilibrium conditions, characterized by static and interconnected fluid phases (Karadimitriou et al., 2014).

$$\Delta P = \mathrm{P_{inlet}} - \mathrm{P_{outlet}} = \mathrm{P_c}(\mathrm{S^w}) \tag{5.4}$$

All of the experiments presented in this project were conducted under dynamic conditions, maintaining a given constant flow rate during the entire test. I use the measured total pressure drop between the inlet and the outlet as the macroscopic capillary pressure in the system. Konangi et al, (2021) presented in Eq. 5.5, how the measured pressure drop in a non-equilibrium system, measured while the fluids are constantly being injected, includes the viscous effect ($\mathrm{P_{viscous}}$) additional to the pore-scale capillary pressure ($\Delta P^{interface}$).

$$\Delta P = \Delta P^{interface} + \mathrm{P_{viscous}} \tag{5.5}$$

Given the viscous effect added in Eq. 5.5, our experiments present a dependence on the flow rates. This effect is explored by injecting at two different flow rates in the Tuscaloosa sample.

5.4. RESULTS AND DISCUSSION

This section presents the two-phase flow experiments performed using the real rock micromodels, materials and experimental setup described in chapters 3 and 4. Results show the capillary pressure curves obtained at different capillary numbers during drainage process for a capillary dominated flow regime. The experiments were conducted under constant injection rate.

5.4.1. Saturation and pressure evolution with time

The wetting fluid saturation (S_w) behavior with time is shown in Fig. 29. At the beginning of each experiment, the saturation S_w starts at 1.0 (i.e., the micromodel is completely saturated with the wetting fluid). As time progresses, S_w decreases with time in all cases. This rate of decrease is proportional to the injection flow rate. For example, S_w in the Tuscaloosa sample decreases much faster when the injection rate is 50 μL/min (micromodel # 2) relative to 5 μL/min (micromodel # 3) (Fig. 29, light grey markers). In the case of the micromodel fabricated with Berea and tested with an injection rate of 50 μL/min (micromodel # 1), the decrease in S_w occurs at a slightly lower rate compared to the Tuscaloosa case obtained at the same rate (Fig. 29, black circles).

The wetting fluid saturation reaches a constant value with time. In the case of the Tuscaloosa sample, the saturation decreased to 0.17 and 0.2 for the 50 and 5 μL/min injection rate, respectively. For the Berea sample case, the residual saturation at long times is 0.26. For the tests conducted at 50 μL/min, this constant saturation state is reached at ~10 minutes. For the test at 5 μL/min, the time required to reach the residual saturation is ~40 minutes. This implies the times to reach the residual saturation is four times longer when the flow rate is reduced tenfold.

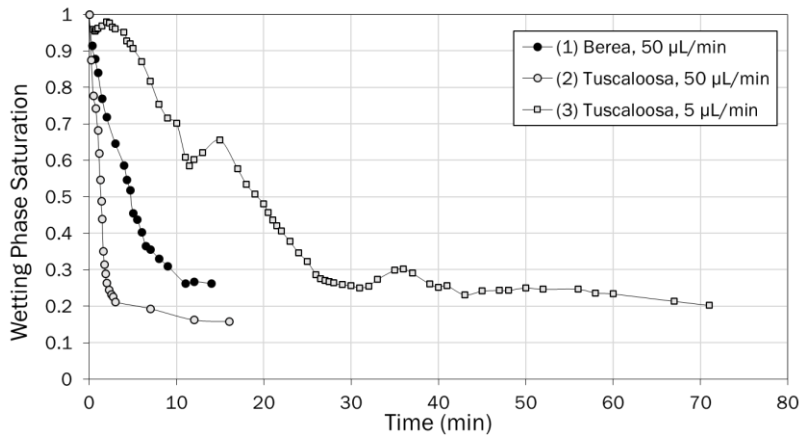

Figure 29: Evolution of wetting phase saturation with time in the micromodel drainage tests conducted at different flow rates using Tuscaloosa and Berea sandstone samples.

The pressure difference across the micromodel changes throughout the drainage test (Fig. 30). As time increases, the pressure vs. time monotonically increases when the injection rate is 50 μL/min (Fig. 30, micromodels # 1 and 2). Conversely, the pressure increase is more erratic at the low injection rate of 5 μL/min (Fig. 30, micromodel # 3). I interpret this irregular increase at low flow rates is caused by the dominance of capillary-flow regime and the dominance of interfacial pressure (i.e., capillary pressure), controlled by the pore space heterogeneity.

When pressure evolution with time is compared at the same injection rates, the rate of pressure drop is faster in the Berea sample. For example, the pressure drop reaches 100 kPa after ~3 min in the Berea sandstone (micromodel # 1) whereas the same pressure of 100 kPa in the Tuscaloosa sandstone (micromodel # 2) takes 15 min.

The pressure response depends highly on flow rate. In the Tuscaloosa samples, the pressure drop reaches 110 kPa at the highest injection rate (micromodel # 2). In comparison, the pressure drop only goes to 7 to 8 kPa at the lowest injection (micromodel

3). I interpret that these pressure differences are attributed to the viscous pressure drop. At high flow rates, the term $P_{viscous}$ in Equation 5.5 is larger relative to the case when the injection flow rate is low, which results in an overall larger measured pressure drop for micromodel # 2.

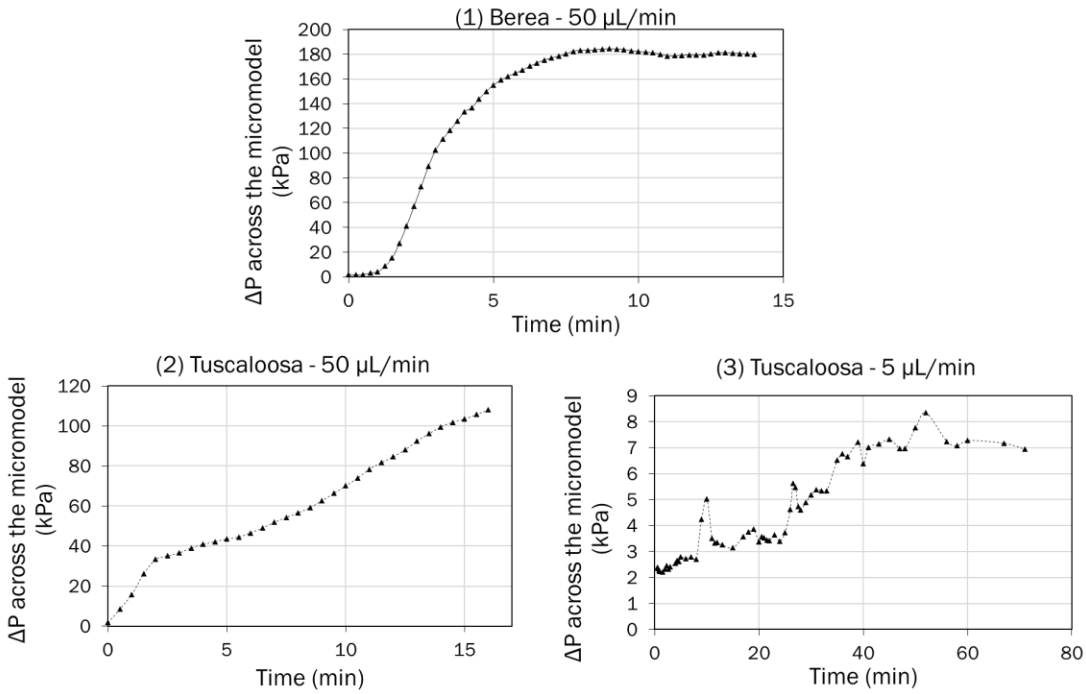

Figure 30: Pressure drop across the micromodel with time in the drainage tests conducted at different flow rates using Tuscaloosa and Berea sandstone samples.

5.4.2. Capillary pressure vs. saturation

The pressure drop across the micromodel (ΔP) and wetting phase saturation (Sw) can be used to infer the dynamic capillary pressure vs. saturation curve. To derive this relationship, I cross plotted ΔP vs. Sw obtained at a given time using data shown in Fig. 29 and 30. Fig. 31 shows these relationships for the three tests. In all cases, as the wetting saturation decreases, the pressure across the micromodel increases. For the tests conducted

using the Tuscaloosa samples, a small decrease in the wetting fluid saturation causes a large increase in pressure drop. This pressure drop value remains approximately constant until the saturation Sw decreases to 0.21 and 0.29 for the 50 μL/min and 5 μL/min test, respectively (Fig. 31, micromodel # 2 and 3). Conversely, in the Berea sandstone test, ΔP increases gradually with decreases in Sw (Fig. 31, micromodel # 1).

The behavior of the ΔP vs. S_w curve at low saturation is different in the Berea and Tuscaloosa samples. For example, the Tuscaloosa sample exhibits a residual wetting phase saturation of Sw = 0.2; increases in pressure (ΔP) above 40 kPa (Fig. 31, micromodel # 2) and 4 kPa (Fig. 31, micromodel # 3) do not further decrease the wetting phase saturation. This behavior is different from that of the Berea sandstone, where the wetting phase saturation seems to decrease at a constant ΔP of 180 kPa (Fig. 31, micromodel # 1).

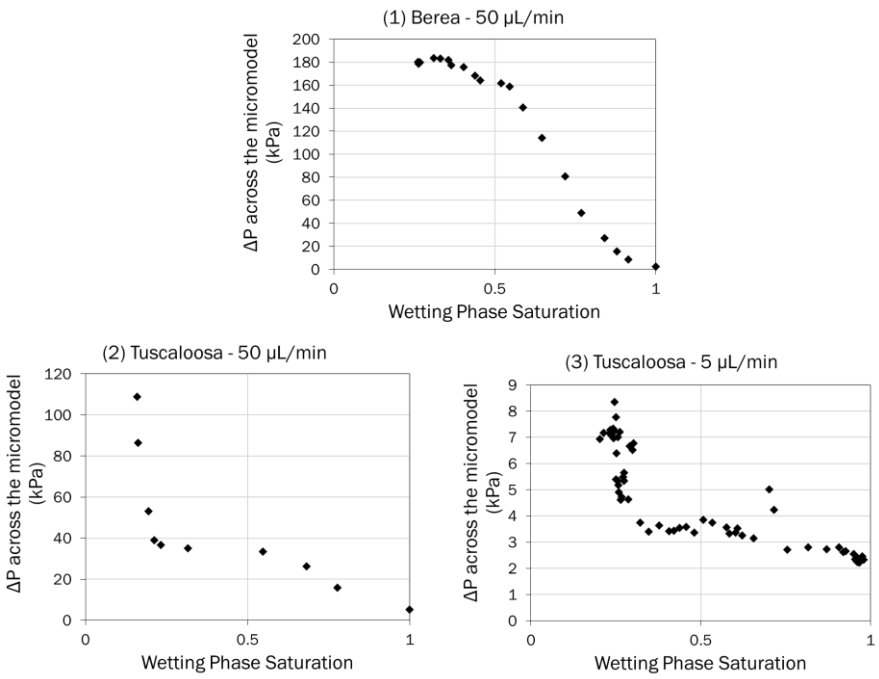

Figure 31: Pressure drop across the micromodel ΔP versus wetting phase saturation Sw for the tests conducted in Berea and Tuscaloosa samples. Two flow rates were used for the Tuscaloosa sample tests.

The pressure drop across the micromodel ΔP varies significantly with flow rate for the Tuscaloosa samples (Fig. 31, micromodel # 2 and 3). Then, to compare tests at different flow rates, I normalized the ΔP with the injection rate q. This is similar to using inverse injectivity index definition, which typically remains constant within short periods of time. Fig. 32 shows the evolution of this normalized ΔP/q with wetting phase saturation Sw for all tests. The Berea sandstone sample displays higher ΔP/q values with respect to the Tuscaloosa sample. Surprisingly, for the two tests conducted using Tuscaloosa samples, the two curves overlap each other (Fig. 32, red and blue markers).

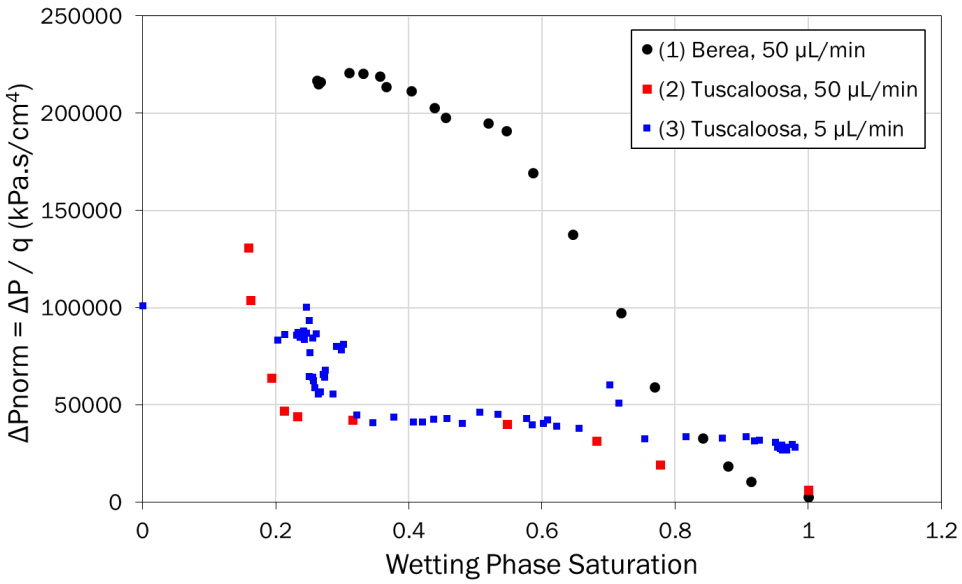

Figure 32: Normalized pressure drop relative to the injection flow rate ΔP/q as a function of wetting phase saturation Sw. The two tests conducted in Tuscaloosa samples are shown.

5.4.3. Discussion

The experimental results shown in Fig. 31 and 32 are derived for pressure drop ΔP and saturation Sw. However, the ΔP vs. Sw data displays similar S-shape, typically observed in capillary pressure (Pc) against saturation data. To explore this observation

further, I can analyze the normalized pressure drop ΔP/q for the Tuscaloosa samples (Fig. 32, blue and red markers). The two curves are obtained at tenfold difference in flow rate; however, they depict similar trends. Capillary pressure is a function of flow rate, but this approach to analyze the shape of the ΔP/q vs. Sw is comparable to the Pc vs. Sw curves while minimizing the effect of various flow rates. This shows that even though the injection rates are changing, the overall trends are not changing, which potentially would mean that they're still in the capillary dominated regime. If in higher flow rates the flow regime was different, then potentially these curves should not have followed the same trend.

I compare the capillary pressure curves for Tuscaloosa sandstone obtained using our microfluids approach against core-scale tests (Fig. 33). The capillary pressures from the micromodel data (Fig. 33, red markers) and core-scale data (Fig. 33, black and empty markers) differ in magnitude; thus, I use two different vertical axes to compare the various curves. Furthermore, the different datasets are obtained at different fluid conditions and the various Tuscaloosa sandstones have slightly different properties. For example, I have used analog fluids to water-scCO_2 system whereas Krevor et al. (2012) core-scale data was obtained using mercury injection porosimetry and Bakhshian et al. (2020) used supercritical CO_2 and brine. Similarly, the Tuscaloosa sample I used is from a core at 10,447 ft and has a porosity of $\phi = 18.8\%$. Krevor et al. (2012) and Bakhshian et al. (2020) samples correspond to depths of 10,499 ft ($\phi = 23.6\%$) and 10,464 ft ($\phi = 28.7\%$), respectively.

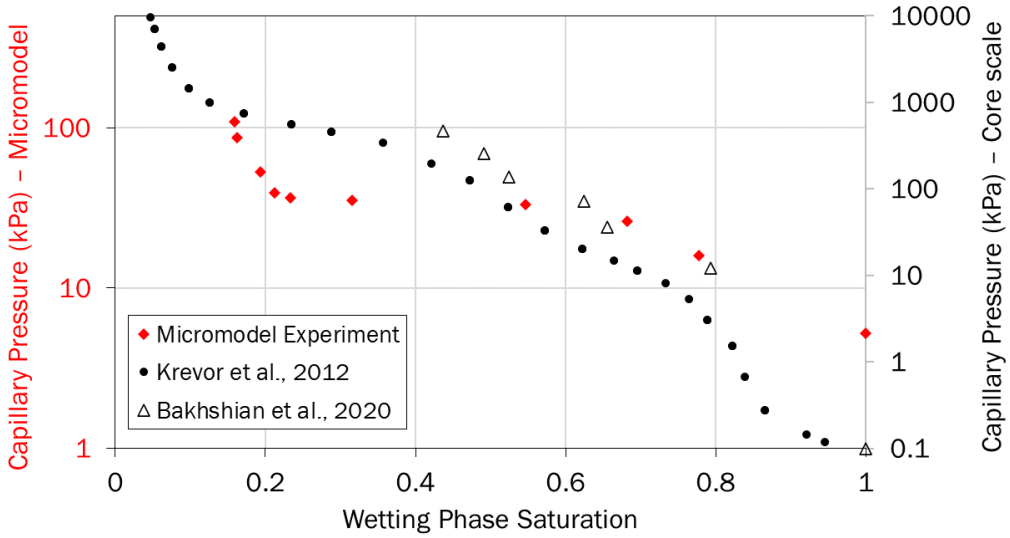

Figure 33: Comparison of capillary pressure curves for Tuscaloosa samples derived using microfluidics (red markers) and core-scale: mercury injection porosimetry (black markers – Krevor et al. 2012) and centrifuge testing (empty markers – vertical sample 2, Bakhshian et al. 2020).

The core-scale mercury injection data from Krevor et al. (2012) shows two distinct decreases in the Pc vs. S_w slope at S_w = 0.65 and 0.30. Similarly, the microfluidics data partially depict these two decreases in the Pc vs. S_w slope at S_w = 0.8 and 0.3. Data gathered by Bakhshian et al. (2020) using the centrifuge method show a Pc vs. S_w plateau at S_w = 0.7. In this case, the residual wetting phase saturation is ~0.4 and there is no Pc vs. Sw information at low saturation values. The Tuscaloosa sample used in this thesis is characterized by having two distinct layers. For example, Fig. 24 shows the micromodel photograph of the Tuscaloosa sample, where the presence of two layers is evident. I interpret that for my data, these two decreases in the Pc vs. Sw slope can be attributed to two distinct layers with different pore sizes. Furthermore, it is clear the scale of these layers

is smaller than the micromodel size (Fig. 24); thus, my micromodel designs using real rocks considers the representative elementary volume to infer Pc vs. S_w curves.

The real rock microfluidics technique shown in this thesis involves a number of steps. I fine-tuned the parameters involved in these steps for the Berea and Tuscaloosa samples. For example, the surface polishing procedure was designed to create a glass-mirrored finish, needed for bonding the PDMS with the rock slice. However, this polishing procedure may not be applicable for other type of materials, including more porous rocks or those with different mineral composition. Thus, I anticipate a trial and error step to adapt the procedure accordingly whenever other materials are used. Alternatively, rocks can be scanned using micro CT to create a digital analog of the porous structure. Then, microfluidics based on this digital image can be made using silicon, which offers well-established fabrication protocols. This approach could be useful if wettability effects or fluid-rock interaction are not considered. However, silicon micromodels have a finite resolution, which limits the minimum pore size they can resolve. This limitation could potentially result in bias estimates of capillary behavior. Ultimately, each technique involves tradeoffs in fabrication, and the choice of technique should be guided by the physicochemical phenomena under investigation.

Chapter 6: Reservoir Characterization in Current CCS Policies

The consideration of new and modified policies that support storing CO_2 in saline aquifers plays an important role in the amount of CO_2 that can be stored in the subsurface. Although hydrocarbon reservoirs have proven the ability to contain fluids for millions of years, a larger storage potential is located in underground brine reservoirs. Saline aquifer formations surpass depleted oil and gas reservoirs by a difference of orders of magnitude: 205 billion metric ton vs. 8,328 billion metric ton, respectively (Fig. 34). This high availability makes saline aquifers an optimal possibility to store large amounts of supercritical CO_2 for geological times (Dooley et al., 2004). Although most CCS policies account for depleted oil and gas reservoirs, the main focus of current studies and permits lay on obtaining information about carbon storage in saline aquifers.

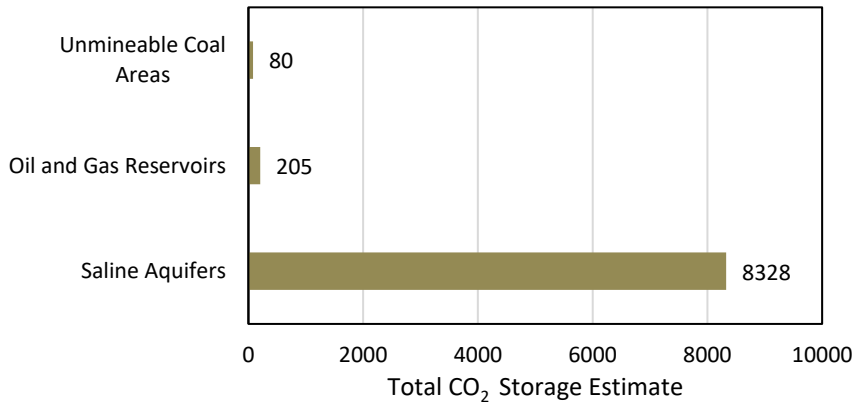

Figure 34: Total CO_2 Storage Resource Estimates (Billion metric tons of CO_2) using the medium scenario = p50. (U.S. Carbon Storage Atlas, 2014).

Saline aquifers offer a promising option for GCS because additional to the large storage capacity and widespread availability, they have minimal impact on freshwater resources. To this end, the characterization of saline aquifers plays an important role in CCS policies. Recent efforts have been made to characterize leak-proof formations of

interest and demonstrate subsurface characteristics that allow the CO_2 to remain trapped for geologic timescales. The U.S. Department of Energy (DOE) has released modifications to the Inflation Reduction Act (IRA) in order to support GCS and impulse geologic characterization of potential storage sites.

As mentioned in previous sections, geologic characterization of reservoirs provides critical information to identify and evaluate potential storage sites. Understanding the rock and fluid properties of the reservoir allows the development of injection strategies that maximize CO_2 storage capacities and minimize the risk of leakage. Fluid flow studies at different scales can help identify optimal injection rates and understand pressure changes in the system, influencing the residual CO_2 saturation in GCS. For example, sand tank tests (Ni & Meckel, 2021), core-scale (Bakhshian et al. 2020), pore-scale modeling (Bakhshian et al. 2019, Bakhshian et al., 2020, Bakhshian 2021) and the micromodel experiments shown in this thesis have attempted to optimize the injection strategy and enhance the storage efficiency. Thus, a good understanding of the reservoir characteristics ensures a better approach of the long-term stability of CO_2 storage.

Subsurface studies also have an important impact on understanding of how geologic features and structures inside and surrounding the area of interest can influence storage in long-term. For example, the presence of faults that could potentially act as closed boundaries in our area or transmissive and connected fracture sets that could lead to CO_2 leakage, as well as mineral precipitation in these fractures that could reduce porosity/permeability with time.

6.1. CAPILLARY PRESSURE MEASUREMENTS IN THE UIC CLASS VI PERMIT

The Class VI Underground Injection Control (UIC) Program from the U.S. Environmental Protection Agency (EPA) regulates the injection of CO_2 into deep underground rock formations with the purpose of long-term carbon storage (Wilson et al., 2008). Capillary pressure is a critical component for the application to the Class VI UIC program. Since the capillary pressure is related to the ability of a porous rock formation to hold fluids, understanding this parameter helps provide information about fluid flow in the porous medium, which allows the permit application to demonstrate if the area of interest is suitable for long-term storage of CO_2.

To model the potential for CO_2 storage, it is important to measure and understand the capillary pressure of the formation. The capillary pressure is generally measured experimentally, and this measurement is used to understand fluid flow at higher scales, such as reservoir scales, by using the value as an input in the modeling tools. Reservoir modeling supports several aspects of the required characterization that need to be included in the permit application. Components include (1) geologic characterization, which is a detailed description of the geologic setting, stratigraphy and structural features, mineralogy and petrophysical properties (i.e., porosity and permeability) that can affect the permeability and storage capacity of the formation, (2) fluid characterization, which involves analyzing the fluid density, interfacial tension, and compressibility, and (3) fluid-rock reactivity and wettability.

Capillary pressure curves obtained from micromodels hold the potential to improve our ability to develop accurate and fast models for two-phase fluid flow. However, as seen in this thesis, they require extensive sample preparation and advanced soft lithography techniques. The capillary pressure work I present here suggests that micromodel techniques

offer complementary pore-scale information to current core-scale capillary pressure methods (e.g., mercury intrusion, core flooding). The combination of these different techniques allows to obtain valuable information at multiple scales. The improvement micromodel fabrication using real rocks would contribute to a more comprehensive understanding of the dynamics involved in fluid displacement processes, allowing for more reliable predictions and insights into the behavior of two-phase flows in GCS applications.

6.2. CARBON STORAGE IN THE OFFSHORE US GULF OF MEXICO

The U.S. Congress, through the Infrastructure Investment and Jobs Act, has assigned the Bureau of Ocean Energy Management (BOEM) and the Bureau of Safety and Environmental Enforcement (BSEE) with the responsibility of leasing the offshore for activities related to the injection of CO_2 into subsurface geologic formations (Celata, 2022). The comprehensive considerations and regulatory framework development highlight the importance of responsible and sustainable implementation of GCS activities offshore.

BOEM and BSEE play a crucial role as landowners and protectors of offshore resources. They have the responsibility to balance the economic development of these resources with the protection of the environment and the well-being of communities. Their needs include effective regulatory oversight, responsible resource management, safety enforcement, long-term planning, and engagement with stakeholders to ensure sustainable and responsible use of the offshore resources.

BOEM, in particular, is involved in leasing offshore areas for various activities, including now GCS. They will conduct the leasing processes, considering factors such as technical feasibility, economic viability, and environmental impact (Batum, 2022). One key aspect involves the understanding of resources as potential storage sites. For this,

geologic characterization is crucial. Conducting leases requires a comprehensive understanding of how the injected CO_2 plume behaves over time to prevent undesirable outcomes such as migration beyond intended areas or unintended environmental impacts. This understanding ensures that the leasing process considers a detailed study of the subsurface area of interest, including predictions of how the CO_2 will migrate during and after injection.

Relative permeability and capillary pressure curves determine the plume stabilization during and after CO_2 injection. They influence the trapping mechanism, reservoir saturation, and pressure response, and CO_2 plume evolution over time. In a buoyancy-dominated flow regime, CO_2 tends to follow paths with smaller capillary entry pressures. The capillary pressure curve characterizes the capillary trapping mechanism, explaining how CO_2 becomes immobile when encountering regions with high capillary entry pressures (Ulfah, 2021).

As BOEM and BSEE proceed with rulemaking and lease design, they will need to incorporate the most reliable methodologies to characterize the subsurface rocks. With the work presented in this thesis, I offer a novel and fast method to determine capillary pressure using real rock micromodels. The model allows to directly visualize the flow behavior while capturing the capillary pressure vs. saturation trends.

Chapter 7: Conclusions and Future Work

7.1. CONCLUSIONS

The goal of this master's thesis was to develop and test a technique for exploring flow behavior at the pore-scale using real rock microfluidics (RRMM) in sandstones. This thesis emphasized the prediction of capillary pressure versus saturation in the context of geological carbon sequestration (GCS). The data shown here, under certain conditions, is able to reproduce the capillary behavior observed in core-scale samples. This thesis is the first one to develop a RRMM technique using sandstones for GCS, allowing future studies to be made with this experimental approach.

I developed a method that creates real rock microfluidics from intact sandstones by combining thin section and soft lithography protocols. This protocol underwent multiple iterations, from grain packed micromodels to the final thin section-based design. To create the RRMM, (1) I cut a ~2.5 cm rectangular piece from a core plug, (2) attach it to a glass sheet, (3) cut and polish to reduce its thickness to ~500 µm, (4) detach the "thick section" from the glass, (5) plasma-bond a polymer-based (PDMS) frame that allows fluid injection, (6) seal the edges with concurrent PDMS injection and curing.

The fabrication procedure was optimized to minimize the likelihood of "thick section" breakage, fluid leaks, accidental detaching of the PDMS with the rock (i.e., PDMS bonding). For example, attaching the rock piece to a glass sheet increases the rigidity of the assembly during reduction of the thin section thickness. Furthermore, the simultaneous injection and curing of the PDMS while sealing the edges as well as assembling the device with polycarbonate sheets and clamps, reduces side-leakage and limits PDMS flow into the micromodel.

I conducted fluid flow experiments in RRMM using Tuscaloosa and Berea sandstone samples and used analog fluids to match the supercritical CO_2 and brine properties (e.g., interfacial tension and viscosity ratios). Using fluorescence microscopy, I derived capillary pressure versus saturation curves. I calculated fluid saturations based on the light intensity and pressure drop measurements across the micromodel.

Our experimental results heavily depend on the injection flow rate of the $scCO_2$ analog; however, for Tuscaloosa samples, when normalized with flow rate the curves collapse into a single trend. This implies our micromodel-based approach is useful to determine the behavior of capillary pressure with saturation.

Our experimental results were compared with core-scale measurements. It is important to consider the scale of heterogeneities present in the rock. Micromodel-based capillary pressure determination is a useful approach when the size of the heterogeneities is smaller than the micromodel size.

The real rock microfluidics technique detailed here involves parameter fine-tuning for Berea and Tuscaloosa samples. For example, the surface polishing procedure may be different for different materials. Trial and error could be expected when working with other rocks. While well-established silicon-based micromodels based on X-ray CT images of real rocks can be used when rock-fluid interactions are not considered, they have limited resolution, potentially biasing capillary behavior estimations. Each microfluidic technique faces inherent tradeoffs. The physical processes under investigation (e.g., wettability effects on capillary behavior) should dictate the choice of the experimental protocol.

Capillary pressure curves impact plume stabilization predictions during and after CO_2 injection. BOEM and BSEE require a detailed analysis of the expected CO_2 flow to minimize the risk of CO_2 migration beyond the intended areas. This thesis presented a

novel real rock microfluidics technique to determine capillary behavior. This can be incorporated into numerical simulators which will guide BOEM and BSEE to conduct more sound decisions when assigning leases or issuing permits.

7.2. FUTURE WORK

As the GCCC group continues to advance this research, there are more processes that can be explored for geological carbon storage. Since I invested a large amount of this project in developing and validating the fabrication method and the experimental setup for the experiments, I recommend that more experiments should be run for different sandstone rocks, covering a wide range of porosities and properties. This will inform if the procedures developed here are valid under various conditions. For example, unconsolidated samples may require a different approach to create the thin sections, or rocks with small pore sizes may need stronger seals to satisfy the high-pressure requirements for injection.

One critical aspect of our experimental protocol was the optimization of the experimental conditions. For the PDMS bonding, it can be difficult to create a sufficiently polished surface for the oxygen plasma to interact with the PDMS surface and form a strong bond. Alternatively, an adhesive material can be used to attach PDMS and polished sandstone surfaces together. Similarly, I observed the PDMS swells when in contact with heptane for prolonged times. I empirically optimized the time for injection to avoid this effect. A future test would be to obtain the immerse the PDMS into heptane and monitor the swelling with time, and an additional recommendation is to further explore other analogue fluids and alternatives for PDMS (other soft materials).

The overall fabrication procedure created in this thesis is more time-consuming than conventional silicon or glass micromodel fabrication, and obtaining results can take

much longer as well. The procedure could be improved by using additional equipment, such as, an automatic thin section machine and trying an automatic polishing procedure.

I use fluid analogues to replicate the supercritical CO_2 and brine system. However, this approach may not fully represent all of the physical and chemical properties during CO_2 injection. For example, dissolution of CO_2 into brine is not equivalent to the dissolution of heptane into the glycerol mixture. To fully investigate if this has a critical effect, results obtained with analog fluids can be compared to supercritical CO_2 and brine using micromodel experiments that tolerate high pressure and temperature (e.g., silicon micromodels).

This thesis focused on capillary vs. saturation trends. However, equally important are the chemical processes during CO_2 injection. For example, brine dry out can be explored using RRMM, with the advantage of using realistic mineral-fluid interactions. This type of study will elucidate the impact of salt precipitation for flow assurance during CO_2 injection projects.

Finally, our experimental results can be complemented with numerical simulations. The sandstone thin section can be scanned to generate a computational mesh and feed experimental results to 3D pore-scale fluid flow models. This will help identify the physical processes that are more relevant for CO_2 injection.

References

Abdoulghafour, H., Sarmadivaleh, M., Hauge, L. P., Fernø, M., & Iglauer, S. (2020). Capillary pressure characteristics of CO2-brine-sandstone systems. *International Journal of Greenhouse Gas Control*, *94*, 102876.

Al-Yaseri, A., Abbasi, G. R., Yekeen, N., Al-Shajalee, F., Giwelli, A., & Xie, Q. (2022). Effects of cleaning process using toluene and acetone on water-wet-quartz/CO2 and oil-wet-quartz/CO2 wettability. *Journal of Petroleum Science and Engineering*, *208*, 109555.

Amarasinghe, W., Farzaneh, S., Fjelde, I., Sohrabi, M., & Guo, Y. (2021). A visual investigation of CO2 convective mixing in water and oil at the pore scale using a micromodel apparatus at reservoir conditions. *Gases*, *1*(1), 53-67.

Aminu, M. D., Nabavi, S. A., Rochelle, C. A., & Manovic, V. (2017). A review of developments in carbon dioxide storage. *Applied Energy*, *208*, 1389-1419.

Armstrong, R. T., Berg, S., Dinariev, O., Evseev, N., Klemin, D., Koroteev, D., & Safonov, S. (2016). Modeling of pore-scale two-phase phenomena using density functional hydrodynamics. *Transport in Porous Media*, *112*, 577-607.

Aryana, S. A., & Kovscek, A. R. (2012). Experiments and analysis of drainage displacement processes relevant to carbon dioxide injection. *Physical Review E*, *86*(6), 066310.

Bachu, S. (2003). Screening and ranking of sedimentary basins for sequestration of CO2 in geological media in response to climate change. *Environmental Geology*, *44*(3), 277–289.

Bakhshian, S., Hosseini, S. A., & Shokri, N. (2019). Pore-scale characteristics of multiphase flow in heterogeneous porous media using the lattice Boltzmann method. *Scientific reports*, *9*(1), 3377.

Bakhshian, S., Hosseini, S. A., & Lake, L. W. (2020). CO2-brine relative permeability and capillary pressure of Tuscaloosa sandstone: Effect of anisotropy. *Advances in Water Resources*, *135*, 103464.

Bakhshian, S., Rabbani, H. S., Hosseini, S. A., & Shokri, N. (2020). New insights into complex interactions between heterogeneity and wettability influencing two-phase flow in porous media. *Geophysical Research Letters*, *47*(14), e2020GL088187.

Bakhshian, S. (2021). Dynamics of dissolution trapping in geological carbon storage. *International Journal of Greenhouse Gas Control*, *112*, 103520.

Bakhshian, S., Hosseini, S. A. (2021). Pore-scale study of capillary and dissolution trapping of CO2 in saline aquifers. *15th International Conference on Greenhouse Gas Control Technologies.* https://ssrn.com/abstract=3816758.

Batum, M. Bureau of Ocean Energy Management (BOEM). (2022). Carbon Sequestration on the Outer Continental Shelf. Retrieved from: https://www.boem.gov/sites/default/files/documents//BOEM%20OCS%20CS%20DOE-NETL%20Carbon%20Meeting%202022.pdf

Benson, S. M., & Cole, D. R. (2008). CO2 sequestration in deep sedimentary formations. *Elements, 4*(5), 325–331.

Berg, S. & Ott, H. (2012). Stability of CO2–brine immiscible displacement. International *Journal of Greenhouse Gas Control, 11,* 188-203.

Berger, P. M., Yoksoulian, L., Freiburg, J. T., Butler, S. K., & Roy, W. R. (2019). Carbon sequestration at the Illinois Basin-Decatur Project: experimental results and geochemical simulations of storage. *Environmental Earth Sciences, 78*, 1-10.

Blunt, M. J. (2017). Multiphase flow in permeable media: A pore-scale perspective. Cambridge university press.

Bostanci, S. C., Limbachiya, M., Kew, H. (2018). Use of recycled aggregates for low carbon and cost-effective concrete construction. *Journal of Cleaner Production, 189*, 176-196.

Brown, M.A. & Li, Y. (2019). Carbon pricing and energy efficiency: pathways to deep decarbonization of the US electric sector. *Energy Efficiency 12*, 463–481.

Bruant, R.G., Jr. J., Celia, M.A., Guswa, A.J., Peters, C.A. (2002). Safe Storage of CO2 in Deep Saline Aquifiers. *Environmental Science & Technology., 36*(11), 240A–245A.

Buchgraber, M., Al-Dossary, M., Ross, C.M. & Kovscek, A.R. (2012). Creation of a dual-porosity micromodel for pore-level visualization of multiphase flow. *Journal of Petroleum Science and Engineering 86*, 27-38.

Buchgraber, M., Kovscek, A. R., & Castanier, L. M. (2012). A study of microscale gas trapping using etched silicon micromodels. *Transport in porous media, 95*, 647-668.

Campbell, B. T., & Orr, F. M. (1985). Flow visualization for CO2/crude-oil displacements. *Society of Petroleum Engineers Journal, 25*(05), 665-678.

Celata, M. U.S. Department of the Interior & Bureau of Ocean Energy Management (BOEM). (2022). Offshore Carbon Storage. Retrieved from: https://www.boem.gov/sites/default/files/documents/about-boem/regulations-guidance/BOEM-5th-International-Conference.pdf

Chang, C., Zhou, Q., Oostrom, M., Kneafsey, T. J., & Mehta, H. (2017). Pore-scale supercritical CO2 dissolution and mass transfer under drainage conditions. *Advances in Water Resources, 100*, 14-25.

Chang, C., Zhou, Q., Kneafsey, T. J., Oostrom, M., & Ju, Y. (2019). Coupled supercritical CO2 dissolution and water flow in pore-scale micromodels. *Advances in Water Resources, 123*, 54-69.

Chatenever, A., & Calhoun Jr, J. C. (1952). Visual examinations of fluid behavior in porous media-part i. *Journal of Petroleum Technology, 4*(06), 149-156.

Chen, S.Y. (2015). The effect of pore size and porosity on capillary pressure in micro porous hydroxyapatite samples. [Master Thesis]. *University of Illinois at Urbana-Champaign*. https://core.ac.uk/download/pdf/158312239.pdf.

Chuoke, R. L., Van Meurs, P., & van der Poel, C. (1959). The instability of slow, immiscible, viscous liquid-liquid displacements in permeable media. *Transactions of the AIME, 216(*01), 188-194.

Churcher, P. L., French, P. R., Shaw, J. C., & Schramm, L. L. (1991, February). Rock properties of Berea sandstone, Baker dolomite, and Indiana limestone. In *SPE International Conference on Oilfield Chemistry* (pp. SPE-21044). SPE.

Cinar, Y., Riaz, A., & Tchelepi, H. A. (2009). Experimental study of CO2 injection into saline formations. *Spe Journal, 14*(04), 588-594.

Diaspro, A., Federici, F., & Robello, M. (2002). Influence of refractive-index mismatch in high-resolution three-dimensional confocal microscopy. *Applied optics, 41*(4), 685-690.

Dimou, A. P., Suzuki, A., Menke, H., Maes, J., & Geiger, S. 3D printing-based microfluidics for Geosciences.

Dooley, J. J., Kim, S. H., Edmonds, J. A., Friedman, S. J., & Wise, M. A. (2005). A first-order global geological CO2-storage potential supply curve and its application in a global integrated assessment model. *In Greenhouse Gas Control Technologies 7* (pp. 573-581).

Duffy, D. C., McDonald, J. C., Schueller, O. J., Whitesides, G. M. (1998). Rapid Prototyping of Microfluidic Systems in Poly(dimethylsiloxane). *Anal. Chem., 70*, 23, 4974–4984.

Er, V., Babadagli, T., & Xu, Z. (2010). Pore-scale investigation of the matrix− fracture interaction during CO2 injection in naturally fractured oil reservoirs. *Energy & Fuels, 24*(2), 1421-1430.

Espinoza, D. N., & Santamarina, J. C. (2010). Water-co2-mineral systems: Interfacial tension, contact angle, and diffusion—Implications to co2 geological storage. *Water Resour. Res., 46(*7).

Dooley, J. J., Kim, S. H., Edmonds, J. A., Friedman, S. J., & Wise, M. A. (2005). A first-order global geological CO2-storage potential supply curve and its application in a global integrated assessment model. In *Greenhouse Gas Control Technologies 7* (pp. 573-581).

Ferrari, A., Jimenez-Martinez, J., Borgne, T. L., Méheust, Y., and Lunati, I. (2015). Challenges in modeling unstable two-phase flow experiments in porous micromodels, *Water Resour. Res., 51*, 1381– 1400.

Gershenzon, N. I., Ritzi, R.W., Dominic, D. F., Mehnert, E., Okwen, R. T. (2016). Comparison of CO2 trapping in highly heterogeneous reservoirs with Brooks-Corey and van Genuchten type capillary pressure curves. *Advances in Water Resources, 96*, 225-236.

Gogoi, S., & Gogoi, S. B. (2019). Review on microfluidic studies for EOR application. *Journal of Petroleum Exploration and Production Technology, 9*, 2263-2277.

Gray, G. W., Bruning, K., Miller, C. T. 2019. Non-hysteretic functional form of capillary pressure in porous media, *Journal of Hydraulic Research, 57*:6, 747-759.

Gulf Coast Carbon Center. (n.d.) GoMCarb Study Area. Retrieved on November 20th, 2023 from: https://gccc.beg.utexas.edu/research/gomcarb-studyarea.

Han, W. S., McPherson B. J., Lichtner, P. C., Wang, F. P. (2010). Evaluation of trapping mechanisms in geologic CO2 sequestration: Case study of SACROC northern platform, a 35-year CO2 injection site. *American Journal of Science, 310* (4) 282-324.

Hassan, A.; Yutkin, M.; Chandra, V.; Patzek, T. (2021). Quality Evaluation of Epoxy Pore Casts Using Silicon Micromodels: Application to Confocal Imaging of Carbonate Samples. *Appl. Sci. 11*, 5557.

He, D., Jiang, P., & Xu, R. (2019). Pore-scale experimental investigation of the effect of supercritical CO2 injection rate and surface wettability on salt precipitation. *Environmental Science & Technology, 53*(24), 14744-14751.

Hosseini, S. A., Lashgari, H., Choi, J. W., Nicot, J. P., Lu, J., & Hovorka, S. D. (2013). Static and dynamic reservoir modeling for geological CO2 sequestration at Cranfield, Mississippi, USA. *International Journal of Greenhouse Gas Control, 18*, 449-462.

Hovorka, S. D., Benson, S. M., Doughty, C., Freifeld, B. M., Sakurai, S., Daley, T. M., ... & Knauss, K. G. (2006). Measuring permanence of CO2 storage in saline formations: the Frio experiment. *Environmental Geosciences, 13*(2), 105-121.

Hu, R., Wan, J., Kim, Y., & Tokunaga, T. K. (2017). Wettability impact on supercritical CO2 capillary trapping: Pore-scale visualization and quantification. *Water Resources Research, 53*(8), 6377-6394.

IEA (2021), Global Energy Review 2021, *IEA*. Retrieved from: https://www.iea.org/reports/global-energy-review-2021.

Jadhawar, P., Yang, J., Chapoy, A., & Tohidi, B. (2020). Subsurface carbon dioxide sequestration and storage in methane hydrate reservoirs combined with clean methane energy recovery. *Energy & Fuels, 35*(2), 1567-1579.

Jafari, M., & Jung, J. (2017). Direct Measurement of Static and Dynamic Contact Angles Using a Random Micromodel Considering Geological CO2 Sequestration. *Sustainability 2017, 9*(12), 2352.

Jafari, M., & Jung, J. (2019). Salinity effect on micro-scale contact angles using a 2D micromodel for geological carbon dioxide sequestration. *Journal of Petroleum Science and Engineering, 178*, 152-161.

Jahanbakhsh, A.; Wlodarczyk, K.L.; Hand, D.P.; Maier, R.R.J.; Maroto-Valer, M.M. (2020). Review of Microfluidic Devices and Imaging Techniques for Fluid Flow Study in Porous Geomaterials. *Sensors, 20,* 4030.

Kassa, A.M., Gasda, S.E., Kumar, K., Radu, F.A. (2020). Impact of time-dependent wettability alteration on the dynamics of capillary pressure. *Advances in Water Resources 142,* 103631.

Kazemifar, F., Blois, G., Kyritsis, D. C., & Christensen, K. T. (2015). A methodology for velocity field measurement in multiphase high-pressure flow of CO2 and water in micromodels. *Water Resources Research, 51*(4), 3017-3029.

Kazemifar, F., Blois, G., Kyritsis, D. C., & Christensen, K. T. (2016). Quantifying the flow dynamics of supercritical CO2–water displacement in a 2D porous micromodel using fluorescent microscopy and microscopic PIV. *Advances in Water Resources, 95*, 352-368.

Kim, KY., Han, W.S., Oh, J. (2012). Characteristics of Salt-Precipitation and the Associated Pressure Build-Up during CO2 Storage in Saline Aquifers. *Transp Porous Med 92,* 397–418.

Konangi, S., Palakurthi, N. K., Karadimitriou, N. K., Comer, K., & Ghia, U. (2021). Comparison of pore-scale capillary pressure to macroscale capillary pressure using direct numerical simulations of drainage under dynamic and quasi-static conditions. *Advances in Water Resources, 147*, 103792.

Kordi, Masoumeh (2013). Characterization and prediction of reservoir quality in chlorite-coated sandstones: evidence from the Late Cretaceous Lower Tuscaloosa Formation at Cranfield Field, Mississippi, U.S.A. [Doctoral Dissertation]. The University of Texas at Austin. http://hdl.handle.net/2152/22084.

Krevor, S., Pini, R., Li, B., Benson, S.M. (2011). Capillary heterogeneity trapping of CO2 in a sandstone rock at reservoir conditions. *Geophysical Research Letters., 38*(15).

Krevor, S. C., Pini, R., Zuo, L., & Benson, S. M. (2012). Relative permeability and trapping of CO2 and water in sandstone rocks at reservoir conditions. *Water resources research*, *48*(2).

Krishnamurthy, P. G., DiCarlo, D., & Meckel, T. (2022). Geologic heterogeneity controls on trapping and migration of CO2. *Geophysical Research Letters*, *49*(16), e2022GL099104.

Lenormand, R., Touboul, E., & Zarcone, C. (1988). Numerical models and experiments on immiscible displacements in porous media. *Journal of fluid mechanics*, *189*, 165-187.

Lenormand, R., Zarcone, C., & Sarr, A. (1983). Mechanisms of the displacement of one fluid by another in a network of capillary ducts. *Journal of Fluid Mechanics*, *135*, 337-353.

Lenormand, R., Touboul, E., & Zarcone, C. (1988). Numerical models and experiments on immiscible displacements in porous media. *Journal of Fluid Mechanics*, *189*, 165-187.

Li, Y., Kazemifar, F., Blois, G., & Christensen, K. T. (2017). Micro-PIV measurements of multiphase flow of water and liquid CO 2 in 2-D heterogeneous porous micromodels. *Water Resources Research*, *53*(7), 6178-6196.

Li, Y., Blois, G., Kazemifar, F., Molla, R. S., & Christensen, K. T. (2021). Pore-Scale Dynamics of Liquid CO2–Water Displacement in 2D Axisymmetric Porous Micromodels Under Strong Drainage and Weak Imbibition Conditions: High-Speed μPIV Measurements. *Frontiers in Water*, *3*, 710370.

Likanapaisal, P., Lun, L., Krishnamurthy, P., & Kohli, K. (2023, October). Understanding Subsurface Uncertainty for Carbon Storage in Saline Aquifers: PVT, SCAL, and Grid-Size Sensitivity. In *SPE Annual Technical Conference and Exhibition* (p. D021S020R002). SPE.

Lu, J., Kharaka, Y. K., Thordsen, J. J., Horita, J., Karamalidis, A., Griffith, C., ... & Hovorka, S. D. (2012). CO2–rock–brine interactions in Lower Tuscaloosa Formation at Cranfield CO2 sequestration site, Mississippi, USA. *Chemical Geology*, *291*, 269-277.

Lu, J., Kordi, M., Hovorka, S. D., Meckel, T.A., Christopher, C. A. (2013). Reservoir characterization and complications for trapping mechanisms at Cranfield CO2 injection site. *International Journal of Greenhouse Gas Control 18* (2013) 361–374.

Lun, L. S., Gao, B., Krishnamurthy, P., Kohli, K., & Wattenbarger, R. C. (2023, October). Developing Consistent Relative Permeability and Capillary Pressure Models for Reservoir Simulation of CCS Projects. In *Abu Dhabi International Petroleum Exhibition and Conference* (p. D031S113R002). SPE.

Lv, P., Liu, Y., & Yang, W. (2020). Investigation on CO2 permeation in water-saturated porous media with disordered pore sizes. *Experimental Thermal and Fluid Science, 119*, 110207.

Lv, Q., Zheng, R., Zhou, T., Guo, X., Wang, W., Li, J., & Liu, Z. (2022). Visualization study of CO2-EOR in carbonate reservoirs using 2.5 D heterogeneous micromodels for CCUS. *Fuel, 330*, 125533.

Mahdavi, S., James, L. A., & Johansen, T. E. Pore Scale Investigation of Carbonated Water Injection with and without Gravity.

Mahdavi, S., & James, L. A. (2020). High pressure and high-temperature study of CO2 saturated-water injection for improving oil displacement; mechanistic and application study. *Fuel, 262*, 116442.

Miri, R., van Noort, R., Aagaard, P., & Hellevang, H. (2015). New insights on the physics of salt precipitation during injection of CO2 into saline aquifers. *International Journal of Greenhouse Gas Control, 43*, 10-21.

Ni, H., & Meckel, T. A. (2021). Characterizing the Effect of Capillary Heterogeneity on Multiphase Flow Pulsation in an Intermediate-Scale Beadpack Experiment Using Time Series Clustering and Frequency Analysis. *Water Resources Research, 57*(11), e2021WR030876.

NOAA. Lindsay, Rebecca. (2021). Climate Change: Atmospheric Carbon Dioxide: National Oceanic and Atmospheric Administration. https://www.climate.gov/ news-features/understandingclimate/climate-change-atmospheric-carbon-dioxide.

Nooraiepour, M., Fazeli, H., Miri, R., & Hellevang, H. (2018). Effect of CO2 phase states and flow rate on salt precipitation in shale caprocks—a microfluidic study. *Environmental science & technology, 52*(10), 6050-6060.

Nuske, P., Ronneberger, O., Karadimitriou, N. K., Helmig, R., & Hassanizadeh, S. M. (2015). Modeling two-phase flow in a micro-model with local thermal non-equilibrium on the Darcy scale. *International Journal of Heat and Mass Transfer, 88*, 822-835.

Panwar, N.L., Kaushik S.C., Kothari, S. (2011). Renewable and Sustainable Energy Reviews. Role of renewable energy sources in environmental protection: *A review 15*(3), 1513-1524.

Porter, M.L., Jimenez-Martinez, J., Martinez, R., McCulloch, Q., Carey, J.W., Viswanathan, H.S. (2015). Geo-material microfluidics at reservoir conditions for subsurface energy resource applications. *Lab Chip, 15*, 4044-4053.

Riazi, M., Sohrabi, M., Bernstone, C., Jamiolahmady, M., & Ireland, S. (2011). Visualisation of mechanisms involved in CO2 injection and storage in hydrocarbon

reservoirs and water-bearing aquifers. *Chemical Engineering Research and Design, 89*(9), 1827–1840.

Sayegh, S. G., & Fisher, D. B. (2009). Enhanced oil recovery by CO2 flooding in homogeneous and heterogeneous 2D micromodels. *Journal of Canadian Petroleum Technology, 48*(08), 30-36.

Schindelin, J., Arganda-Carreras, I., Frise, E., Kaynig, V., Longair, M., Pietzsch, T., ... & Cardona, A. (2012). Fiji: an open-source platform for biological-image analysis. *Nature methods, 9*(7), 676-682.

Sell, A., Fadaei, H., Kim, M., & Sinton, D. (2013). Measurement of CO2 diffusivity for carbon sequestration: A microfluidic approach for reservoir-specific analysis. *Environmental science & technology, 47*(1), 71-78.

Seo, S., Mastiani, M., Hafez, M., Kunel, G, Asfour, C. G., Garcia-Ocampo, K. I., Linares, N., Saldana, C., Yang, K., & Kim, M. (2019). Injection of in-situ generated CO2 microbubbles into deep saline aquifers for enhanced carbon sequestration. *International Journal of Greenhouse Gas Control, 83*, 256-264.

Singh, R., Sivaguru, M., Fried, G. A., Fouke, B. W., Sanford, R. A., Carrera, M., Werth, C. J. (2017). Real rock-microfluidic flow cell: A test bed for real-time in situ analysis of flow, transport, and reaction in a subsurface reactive transport environment. *Journal of Contaminant Hydrology, 204*(28-39).

Song, W., De Hass, T. W., Fadaei, H., Sinton, D. (2014). Chip-off-the-old-rock: the study of reservoir-relevant geological processes with real-rock micromodels. *Lab Chip, 14*, 4382-4390.

Tong, M., Li, L., Wang, W., Jiang, Y. (2006). Determining capillary-pressure curve, pore-size distribution, and permeability from induced polarization of shaley sand. *Geophysics 71:* N33-N40.

Ulfah, M. (2021). Plume Migration and Pressure Evolution Analyses for Recommendations in Offshore CO2 Storage Acreage Leasing Policy. [Master Thesis]. The University of Texas at Austin. https://repositories.lib.utexas.edu/items/9e71d578-9ed8-45c9-800d-10577110b96a

U.S. Carbon Storage Atlas (2014). Fifth Edition (Atlas V). NARCARB ATLAS: https://www.netl.doe.gov/coal/carbon-storage/strategic-program-support/natcarb-atlas

Van der Meer, L.G.H., (1995). The CO2 storage efficiency of aquifers. *Energy Conversion and Management 36*(6-9):513-518.

Wang, Y., Zhang, C., Wei, N., Oostrom, M., Wietsma, T. W., Li, X., & Bonneville, A. (2013). Experimental study of crossover from capillary to viscous fingering for

supercritical CO2-water displacement in a homogeneous pore network. *Environmental Science and Technology, 47*(1), 212–218.

Wilson, E. J., Morgan, M. G., Apt, J., Bonner, M., Bunting, C., Gode, J., ... & Wright, I. W. (2008). Regulating the geological sequestration of CO2. https://pubs.acs.org/doi/pdf/10.1021/es087037k

Xiong, L., Chen, P., Zhou, Q. (2014) Adhesion promotion between PDMS and glass by oxygen plasma pre-treatment, *Journal of Adhesion Science and Technology, 28*:11, 1046-1054.

Yiotis, A., Karadimitriou, N.K., Zarikos, I. et al. Pore-scale effects during the transition from capillary- to viscosity-dominated flow dynamics within microfluidic porous-like domains. *Sci Rep 11*, 3891 (2021).

Zhang, C., Oostrom, M., Wietsma, T. W., Grate, J. W., & Warner, M. G. (2011). Influence of viscous and capillary forces on immiscible fluid displacement: Pore-scale experimental study in a water-wet micromodel demonstrating viscous and capillary fingering. *Energy & Fuels, 25*(8), 3493-3505.

Zhang, C., Oostrom, M., Grate, J. W., Wietsma, T. W., & Warner, M. G. (2011). Liquid CO2 displacement of water in a dual-permeability pore network micromodel. *Environmental science & technology, 45*(17), 7581-7588.

Zuo, L., Zhang, C., Falta, R. W., & Benson, S. M. (2013). Micromodel investigations of CO2 exsolution from carbonated water in sedimentary rocks. *Advances in Water Resources, 53*, 188-197.